Summer 8-2019

Spring-Guided Electromagnetic Vibrations Energy Harvester

Ghufran Jaber Aldawood

SPRING-GUIDED ELECTROMAGNETIC VIBRATIONS ENERGY HARVESTER

by

Ghufran Jaber Aldawood, B.S.

A Thesis Presented in Partial Fulfillment
of the Requirements for the Degree
Master of Science

COLLEGE OF ENGINEERING AND SCIENCE
LOUISIANA TECH UNIVERSITY

August 2019

LOUISIANA TECH UNIVERSITY

GRADUATE SCHOOL

June 11, 2019
Date of thesis defense

We hereby recommend that the thesis prepared by

Ghufran Aldawood, B.S.

entitled **SPRING-GUIDED ELECTROMAGNETIC VIBRATIONS ENERGY HARVESTER**

be accepted in partial fulfillment of the requirements for the degree of

Master of Science in Engineering, Electrical Engineering Concentration

Dr. Hamzeh Bardaweel, Supervisor of Thesis Research

Dr. Chester Wilson,
Head of Electrical Engineering

Members of the Thesis Committee:
Dr. Sandra Zivanovic
Dr. Leland Weiss

Approved:

Hisham Hegab
Dean of Engineering & Science

Approved:

Ramu Ramachandran
Dean of the Graduate School

ABSTRACT

In recent years, vibration based energy harvesting techniques showed a promising alternative to power wireless sensor networks (WSN). Billions of low power sensors are currently used widely in wireless sensor networks (WSN) and the Internet of Things environment (IoT). These sensors are currently powered by a traditional power source, i.e. a disposable battery. Vibrations are an abundant source of kinetic energy that can serve as the power source for these sensor nodes. This approach eliminates the necessity for frequent battery replacement due to their short-life span and hazardous disposal process. The adverse and irreversible effect from the disposal of these batteries have an alarming impact on the environment.

In order to limit the severity of this impact, the vibration energy harvesting alternative is proposed as a solution. Vibration energy harvesting provides on site power sources for these small sensors by utilizing kinetic vibrations from its surroundings. This was the drive for much of the research done in vibration based energy harvesting. Most of the work that has been done so far focused on linear resonators with limited operational bandwidth. This limitation opposes a challenge, considering that vibrations exist on a wide frequency spectrum. This challenge was met by the invention of levitation based magnetic energy harvester. In a traditional magnetic levitation design, two stationary magnets are fixated in an orientation to repel a center magnet to allow it to float in between.

This mechanism shows considerable lever in terms of power generation and operational bandwidth over linear counterparts. The traditional design shows superior performance over linear generators. Nonetheless, it remains deficient in power output as well as operational bandwidth. This work introduces an Enhanced Energy Harvester (EEH) design over the traditional design (TEH) based on dual mass moving magnets. The proposed design shows significant increase in power output and a wider frequency response bandwidth. The presented EEH design consists of a levitated magnet, an FR4 spring-guided magnet, and coils. Prototypes of the EEH have been fabricated and characterized experimentally. Nonlinear dynamical models of the EEH are developed and validated against experimental data.

The results show excellent agreement between model simulations and experimental data. The figure of merits shows that the presented EEH design significantly outperforms the commonly studied magnetic spring based vibration energy harvesters. The EEH generates 1.97 mW/cm^3g^2 at 0.4 $g[m/s2]$ which is approximately 400% the amount of power generated by the traditional magnetic spring based harvester, i.e. 0.5 $[mW/cm^3g^2]$. At lower acceleration, i.e. 0.1 $g[m/s2]$, the enhanced harvester exhibits 4000% increase in power density compared to the traditional harvester. This makes the presented enhanced harvester design exceptionally suitable for applications where low acceleration oscillations are abundant, including harvesting vibrations from highway bridges and human body motion. Additionally, the half-power frequency bandwidth of the EEH is 90% wider than the bandwidth of its rival traditional magnetic spring based energy harvester.

APPROVAL FOR SCHOLARLY DISSEMINATION

The author grants to the Prescott Memorial Library of Louisiana Tech University the right to reproduce, by appropriate methods, upon request, any or all portions of this Thesis. It is understood that "proper request" consist of the agreement, on the part of the requesting party, that said reproduction is for his personal use and that subsequent reproduction will not occur without written approval of the author of this Thesis. Further, any portions of the Thesis used in books, papers, and other works must be appropriately referenced to this Thesis.

Finally, the author of this Thesis reserves the right to publish freely, in the literature, at any time, any or all portions of this Thesis.

Author Ghufran Jaber Aldawood

Date 06/30/2019

DEDICATION

To my beloved parents, for they gave up so much of their lives to make sure that I get to live a better one. To my sisters, Hawa, Hasna and Fatma, for all the love, support and motivation.

TABLE OF CONTENTS

ABSTRACT iii

DEDICATION vi

LIST OF TABLES ix

LIST OF FIGURES x

ACKNOWLEDGMENTS xiii

CHAPTER 1 INTRODUCTION 1

1.1 Motivation 1

1.2 Literature Review 2

1.3 Vibration Based Energy Harvesting 4

1.3.1 Piezoelectric Energy Harvesting 6

1.3.2 Electrostatic Energy Harvesting 7

1.3.3 Electromagnetic Energy Harvesting 9

1.3.4 Traditional Magnetic Levitation Energy Harvesters 11

1.4 Objective of the Work 15

1.4.1 Structure of Thesis 16

CHAPTER 2 DESIGN AND FABRICATION 17

2.1 Traditional Energy Harvester and Enhanced Energy Harvester Design 17

2.2 FR4 Springs Design and Fabrication 21

CHAPTER 3 MODEL AND THEORY 22

3.1 Formulation of Magnetic Forces 22

3.2 Equations of Motion 26

3.3 Formulation of Output Voltages from the Harvesters. 27

3.3.1 EEH 27

3.3.2 TEH 30

CHAPTER 4 EXPERIMENT 31

4.1 Overview 31

4.2 Static Characterization 31

4.3 Dynamic Characterization 32

CHAPTER 5 RESULTS AND DISCUSSION 36

5.1 Overview 36

5.2 Force Measurements and Model Validation 36

5.3 Open Circuit Voltage Frequency Response 40

5.4 Power Measurements 44

5.5 Energy Harvester Bandwidth 48

CHAPTER 6 CONCLUSION AND FUTURE DIRECTION 50

APPENDIXA Nomenclature 52

BIBLIOGRAPHY 57

LIST OF TABLES

Table 1.1: Commonly found sources of vibrations 5

Table 2.1: Material parameters and specifications 20

Table 5.1: Normalized power comparison of TEH and EEH. 48

Table A.1: Nomenclature 53

LIST OF FIGURES

Figure 1.1: Schematic of a vibration generator. 6

Figure 1.2: Schematic of vibration based piezoelectric energy harvester..... 7

Figure 1.3: Separation distance variable electrostatic energy harvester. 8

Figure 1.4: Section view of electromagnetic energy harvesting bracelet..... 10

Figure 1.5: Cross-sectional view of a traditional magnetic-levitation based energy harvester. 11

Figure 1.6: (a) Single levitating magnet, (b) two levitating magnets with one separator, (c) three moving magnets with two separators 13

Figure 1.7: Quad-stable energy harvester schematic. 15

Figure 2.1: Exploded view schematic of enhanced versus traditional magnetic spring based energy harvesters: a) TEH and b) EEH. 18

Figure 2.2: Cross-sectional view of design and geometry of the harvesters: a) TEH and b) EEH. 19

Figure 2.3: Fully fabricated and assembled harvesters: a) TEH and b) EEH..... 20

Figure 2.4: FR4 planar springs used in the EEH design: a) First FR4 spring design, b) Second FR4 spring design, c) Third FR4 spring design, and d) Dimensions and geometry. 21

Figure 3.1: Magnetic model representation of the harvesters: a) Force derivation, and b) Voltage derivation. 23

Figure 3.2: Multi-dipole approximation schematic of the levitated magnet..... 25

Figure 3.3: Mechanical model schematic of the harvesters: a) Free body diagram of the TEH and b) Free body diagram of the EEH. 26

Figure 4.1: Experiment apparatus used for measuring restoring forces. 32

Figure 4.2: Ringdown waveforms for (a) TEH, (b) EEH-c, (c) EEH-b, and (d) EEH-d. 33

Figure 4.3: Experiment apparatus used for dynamic characterization of the fabricated harvesters. 34

Figure 4.4: Schematic of experiment setup used for energy harvesters′ power measurements. 35

Figure 5.1: Measured and modeled magnetic spring forces: a) F1 acting on levitated magnet and b) F2 acting on top magnet. 38

Figure 5.2: Measured magnetic spring force acting on the levitated magnet and the error associated with the force values. 39

Figure 5.3: Measured restoring forces of the fabricated FR4-a, FR4-b, and FR4-c springs. 39

Figure 5.4: Forward and backward frequency response of TEH: a) Experiment at 0.3 $g[m/s^2]$, b) model at 0.3 $g[m/s^2]$, c) Experiment at 0.5 $g[m/s^2]$, and d) model at 0.5 $g[m/s^2]$. Experiment: Grey for forward and black for backward. Model: light blue for forward and dark blue for backward. 41

Figure 5.5: Forward and backward frequency response of TEH: a) Experiment at 0.3 $g[m/s^2]$, b) model at 0.3 $g[m/s^2]$, c) Experiment at 0.5 $g[m/s^2]$, and d) model at 0.5 $g[m/s^2]$. Experiment: Grey for forward and black for backward. Model: light blue for forward and dark blue for backward. 42

Figure 5.6: Forward and backward frequency response of EEH with FR4-a spring: a) Experiment at 0.3 $g[m/s^2]$, b) model at 0.3 $g[m/s^2]$, c) Experiment at 0.5 $g[m/s^2]$, and d) model at 0.5 $g[m/s^2]$. Experiment: Middle coil (grey for Forward and black for backward), Top coil (dark brown for forward and light brown for backward). Model: Middle coil (light blue for forward and dark blue for backward), Top coil (dark green for forward and light green for backward). 43

Figure 5.7: Forward and backward frequency response of EEH with FR4-c spring: a) Experiment at 0.3 $g[m/s^2]$, b) model at 0.3 $g[m/s^2]$, c) Experiment at 0.5 $g[m/s^2]$, and d) model at 0.5 $g[m/s^2]$. Experiment: Middle coil (grey for Forward and black for backward), Top coil (dark brown for forward and light brown for backward). Model: Middle coil (light blue for forward and dark blue for backward), Top coil (dark green for forward and light green for backward). 44

Figure 5.8: Power generated by the TEH and EEH (with FR4-a, FR4-b, FR4-c) at different acceleration levels: a) Power generation at 0.1 $g[m/s^2]$, b) Power generation at 0.3 $g[m/s^2]$, and c) Power generation at 0.5 $g[m/s^2]$..... 45

Figure 5.9: Comparison of power generation at different acceleration levels: a) Middle coil in the TEH and EEH, and b) Top coil in EEH..... 46

Figure 5.10: Comparison of bandwidths of traditional and enhanced harvesters at different acceleration levels..... 49

ACKNOWLEDGMENTS

I need thank my chair and advisor Dr. Hamzeh Bardaweel for the indispensable knowledge and constant encouragement that he offered, for being so approachable and, most importantly, for his patience throughout this process. I have highly benefited from his area of expertise as well as learned a great deal about work ethics. Also, I thank my committee members Dr. Sandra Zivanovic and Dr. Leland Weiss for their efforts in proofreading and assessing my thesis. I must thank my friend and lab mate Hieu Nguyen, for his major contribution in the mathematical modeling and guidance in experimental work of this thesis. I am indebted for all the selfless help he provided in both forms of knowledge and encouragement. I also want to thank Mehdi Mofidian for his immense help in the lab and in teaching me how to use most of the lab equipment. I thank Winner Anigbogu for his positive and cheerful attitude. In particular, I need to thank my friend Saleh Bajaba, who offered refuge from the frustrations and challenges that research often brings; his mentorship throughout this process has been vital in getting this thesis work completed. I have also been blessed with my friend Sevda Molani who has been a tremendous source of support and comfort. I thank her for all the guidance she provided in helping me write this thesis in LaTeX.

CHAPTER 1

INTRODUCTION

1.1 Motivation

Internet of Things (IoT) is expected to revolutionize the globe by connecting over 25 billion devices with over six trillion dollars market share in the next five years [1]. With this innovative technology, wireless sensors connected to a network will be able to collect information about the surrounding environment, including temperature, pressure, gas leak, humidity, flow rate, etc. Real-time readings from these sensors will facilitate new business opportunities and solve problems related to global needs such as energy, water, food shortages, green house, and terrorism. Nonetheless, the use of traditional batteries to operate these sensors requires continuous replacement, frequent maintenance, extensive labor, and hazardous disposal [2,3]. This is especially daunting because billions of batteries are needed to power billions of sensors.

However, the continuous drop in power requirements to operate these sensors [4, 5] and other gadgets [6–8] has resulted in a growing interest in utilizing freely available energy sources from the surrounding environment to provide the electric power needed to operate these sensors. Among these alternative sources is ambient vibrations [9] that are made of broadband low frequencies with power densities that can reach approximately 500 $\mu W/cm^3$ [10]. Over the past few decades, much of the work on vibration energy harvesting has focused on linear harvesters to convert the

energy in these vibrations into useful electric power. However, researchers around the globe quickly realized the inherent limitations of a linear energy harvester design.

First, a linear design is only capable of harvesting maximum power at a single frequency, i.e. resonant frequency. Therefore, linear harvesters are inappropriate for most sources of ambient vibrations because these vibrations are on a broadband low frequency spectrum. Second, low frequency operation adds significant challenges to the linear design because it will require an extremely soft spring and large mass. Consequently, recent research efforts have shifted towards intentionally introducing and exploiting nonlinearities into the harvester design to broaden its frequency response. These nonlinearities include geometric nonlinearities [11, 12], stiffness nonlinearities [13–15], and damping nonlinearities [16, 17].

1.2 Literature Review

Information and communication technologies (ICT) emerged at a rapid rate only twenty-five years ago [18], linking millions of people through computers and mobile devices. Currently, ICT is evolving, not only connecting people, but it is connecting objects (cars, buildings, and electrical appliances), thus creating internet of things (IoT) [19]. With the accelerated growth of the revolutionizing technologies of IoT, it is forecasted that over 25 billion of wireless sensors will soon be embedded in most machines, transportation, and around our environment by 2020 [1]. But who is going to change those billions of batteries? Powering these wireless sensors autonomously is still a major challenge that engineers are trying to overcome and is yet to be realized. Applications of IoT are widely used, some are found in factory automation [20], health

monitoring and medical diagnostics [16], security and military unmanned vehicle navigation [21], aircraft fatigue crack detection [10] just to name a few. Companies such as John Deere and UPS currently use IoT-based fleet tracking which gives real-time visibility into vehicle location and route analytics [22]. For instance, currently, one of the most essential IoT technologies are radio frequency identification (RFID). Disney′s new MagicBand wristbands have RFID chips which allow connectivity of the system to connect data (park tickets, hotel room keys, payments) to park visitors [22]. The continuous dimension reduction of CMOS integrated circuitry, and consequently power consumption, has led to this large-scale utilization of wireless sensor and actuator networks [10]. Supplying power to the wireless sensor nodes remains a major challenge in the implementation process [10, 23].

Currently, these low power wireless sensors are powered by conventional batteries that require frequent replacement and extensive labor [24]. This opposes an issue for areas where many of these sensors are implemented, making the replacement impractical. It is especially an issue for sensors located in remote or hazardous areas, where battery replacement can be life threatening [15]. Furthermore, the impact extends beyond impractical or unsafe installation. The batteries' detrimental effect on the environment, specifically RFID tags disposal, is an extensively investigated area of research. Active RFID sensor tags are powered by a traditional on-tag battery. These batteries contain significant amounts of heavy metals that effect the recycling and disposal processes [18].

The European commission had released an action plan in 2009 in reference to IoT technology. Action plan no.12 addressed waste management of RFID tags and

the arising challenge of recycling its complex metal components [19]. The German federal environment agency had also revealed the alarming number of RFID tags that were disposed of in 2009 to be ~ 86 million tags. The agency projects an estimated number of tags to be disposed of by 2020 to reach 23 billion [25]. It is evident from the number of publications, patents, and product prototype throughout the past decade that extensive research in the area of energy harvesting has been made to address the aforementioned battery′s.

The energy harvesting field offered many promising advances showcasing cost effective and energy efficient solutions to power these wireless sensor networks [23]. Of all the energy harvesting solutions proposed, solar energy provides nearly two orders of magnitude higher power density than other energy sources: $15,000\ \mu W/cm^3$ [26]. However, this is not the case for an indoor environment where it drops to $10-20$ $\mu W/cm^3$. The most attractive alternative would be the use of mechanical vibrations which provide power density up to 500 $\mu W/cm^3$ [10, 26].

1.3 Vibration Based Energy Harvesting

The focus here would be on relatively low vibration transducers that can harvest energy from commonly occurring vibrations in the environment. Vibration energy can be converted into electrical energy through three common methods of transduction: piezoelectric [27, 28], electrostatic [29, 30], or electromagnetic [31, 32].

Some common vibration sources and their corresponding acceleration peak magnitudes and dominant frequencies are found in Table 1.1. [9, 33, 34].

Table 1.1 Commonly found sources of vibrations

Vibration Source	**Peak acceleration (g)**	**Frequency (Hz)**
Kitchen blender casing	0.65	121
Clothes dryer	0.35	121
Microwave	0.1	200
Toyota Vios-1.5cc car (stationary)	0.2	25
Base of 3-axis machine tool	1.0	70
Washing machine (unloaded)	0.03	39

These common and periodic vibrations generated by rotating machinery or engines can be tapped to generate power. Therefore, the approach of energy harvesting makes it possible to realize *in situ* energy source that harness the otherwise wasted kinetic energy from vibrations. This gave rise to the vibration based energy harvesting area of the research as a proposed solution to extend wireless sensors' lifetime indefinitely [35].

Vibration energy harvesting occurs in a two-step conversion. Firstly, vibrations turn into a relative motion in a mass-spring system. This is described by the equation of motion and schematic [36, 37]:

$$m\ddot{z}(t) + d\dot{z}(t) + kz(t) + F = -m\ddot{y}(t) \tag{1.1}$$

where the dots represent derivatives with respect to time; m is the seismic mass, and d and k are the mechanical damping and stiffness constants, respectively. The mass m moves with relative displacement $z(t)$ with respect to the housing displacement $y(t)$. The second step of the conversion includes the use of a mechanical-to-electrical converter (piezoelectric material, coil around electromagnet, or variable capacitor), which then converts that motion into electricity [33]. The mechanical-to-electrical conversion introduces an electromechanical coupling effect to the system. This effect is

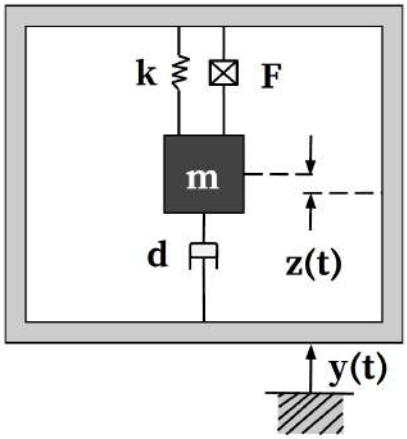

Figure 1.1: Schematic of a vibration generator.

in the form of a mechanical force opposing the relative motion due to Lenz's Law [13]. This electromagnetic interaction between the magnet and the current i is accounted for by the force term F in Equation 1.1 where F is given by [37]:

$$F = \phi i \tag{1.2}$$

where ϕ is the electromechanical coupling coefficient.

1.3.1 Piezoelectric Energy Harvesting

Piezoelectricity is a property of materials that exhibit direct and converse piezoelectric effects. The direct effect is produced when the crystals undergo mechanical deformation allowing electric current generation. The converse effect produces controlled deformation of piezo crystal when electrical charges are applied [38]. The generation of electricity inside the piezoelectric material is proportional to the induced stress [38]. This allows for energy conversion opportunity from surrounding vibrations.

A design of a MEMS piezoelectric energy harvester is depicted in Figure 1.2 [39]. The harvester has an etched spiral structure and is 0.11 mm^3 in size. When

the harvester is subjected to vibrations, the spiral structure will oscillate, thus creating stress on the structure boundaries which allows for induced voltage. Under base

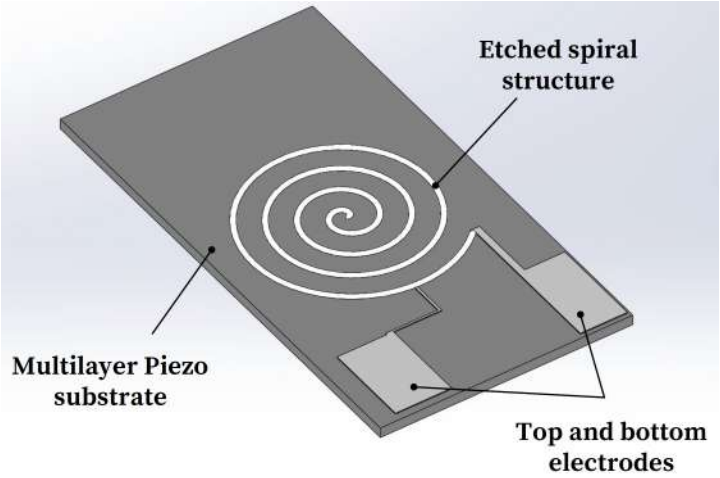

Figure 1.2: Schematic of vibration based piezoelectric energy harvester.

excitation, for low power transducers, piezoelectric harvesters are flexible, lightweight and have an easy mounting process. However, an essential limitation of piezoelectrics is their inherently large internal resistance [24]. Consequently, large load resistance is required to obtain optimum power transfer. This results in very small output currents, i.e. in the order of 1 mA. These currents are well below the threshold required to operate wireless sensors, i.e. 10-50 mA [24].

1.3.2 Electrostatic Energy Harvesting

Electrostatic micro harvesters generate electricity from variations in capacitance between the capacitor plate's surface. A variable capacitor can be utilized in energy harvesting by varying any of these three variables: area, separation distance, or dielectric constant [40]. By maintaining a constant charge value (Q) and voltage (V),

a variation in capacitance (ΔC) results in variations in voltage (Δv) [41]:

$$\Delta C = \frac{Qconst}{\Delta v} \tag{1.3}$$

A vibration based electrostatic energy harvester that relies on separation distance variation can be seen in Figure 1.3 [42]. The micro-machined power generator has a proof mass supported on a flexible polyimide membrane. Gold metal plates were patterned for the fixed and the moving plate to form the parallel plate capacitor. Generation of power is achieved from the mechanical force causing the plates to move apart against the electric field.

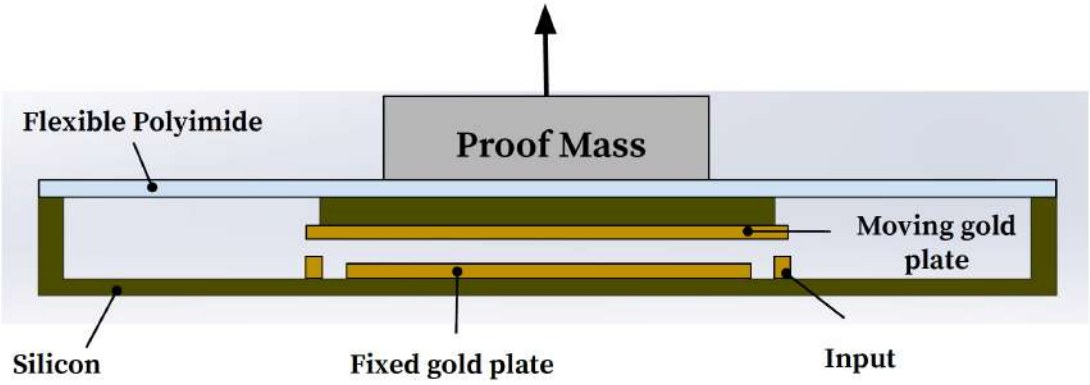

Figure 1.3: Separation distance variable electrostatic energy harvester.

Electrostatic energy harvesters can be easily fabricated on a small scale using MEMS techniques. However, an electric field-based harvester is limited by the maximum allowable electric field without electric breakdown, typically 10^8 V/m for small scale devices [43]. Furthermore, one major and unavoidable problem in fabricating electrostatically actuated devices is known as stiction, a pull-in voltage induced failure. Stiction occurs when the electrostatic force exceeds a certain threshold

causing the capacitor parallel plates to adhere together, resulting in permanent damage to the plates [44].

1.3.3 Electromagnetic Energy Harvesting

The principal for electromagnetic energy harvesting stems from Michael Faraday's Law of electromagnetic induction; any change in the magnetic environment of a coil will cause an electromotive force (voltage) to be induced inside that coil. This phenomenon serves the fundamental basis for electrical generators, motors, transformers, and many other electromagnetic machines [45]. The electromotive force induced inside of the coil is equal to the time rate of change of the magnetic flux linkage in that coil [23], i.e.

$$\varepsilon = -N\frac{d\phi_B}{dt} = \frac{d\mathbf{\Phi}}{dt} \tag{1.4}$$

where N is the number of coil turns, $d\phi_B$ is the average flux linkage per turn, $d\mathbf{\Phi}$ is the total flux linkage given by the summation of linkages of the individual turns [23]:

$$\Phi = \sum_{i=1}^{N} \int_{Ai} B \cdot dA \tag{1.5}$$

Magnetic induction based harvesters can carry adequate power supply in wearable electronics. A human motion based electromagnetic energy harvesting bracelet can be seen in Figure 1.4 [46].

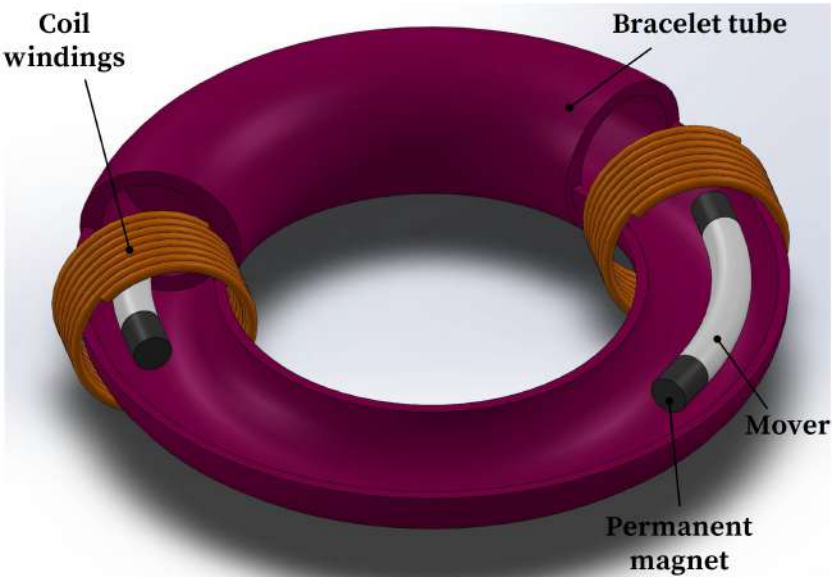

Figure 1.4: Section view of electromagnetic energy harvesting bracelet.

The bracelet harvester uses the motion of permanent magnetic movers to harvest energy from the wearer's motion in any direction. The magnetic movers are packaged in a shell, and repel each other in a rotational motion through the coil transducers. The bracelet harvester can charge a 47 μF-25 V rated capacitor in $\approx$ 132 ms.

Among all the motion based transduction methods, electromagnetic energy harvesting prove to be most effective at generating power at a small scale [47]. Regardless of the mechanism used, most of the work on vibration transducers focused on designing linear resonators that operate in a narrow frequency bandwidth. This does not reflect a realistic environment where frequency of vibrations varies in a certain range. Therefore, it would be more appropriate to take into consideration the systems response to a broader excitation frequency spectrum [48]. Considerable bandwidth enhancements can be achieved by exploiting magnetic levitation-based

energy harvesting techniques. [13, 14, 49–53]. Magnetic levitation system′s exhibit nonlinear negative stiffness profiles. This nonlinearity is a product of the repulsive forces between the magnetic poles, which results in a nonlinear frequency response [14].

1.3.4 Traditional Magnetic Levitation Energy Harvesters

In a traditional magnetic levitation design, stationary magnets are positioned at the ends of a center magnet, as depicted in Figure 1.5. The orientation of the outer stationary magnets are configured to repel the center magnet causing it to float at a stable point (mono-stable), and therefore become suspended by nonlinear restoring forces [11–13, 49, 50, 54].

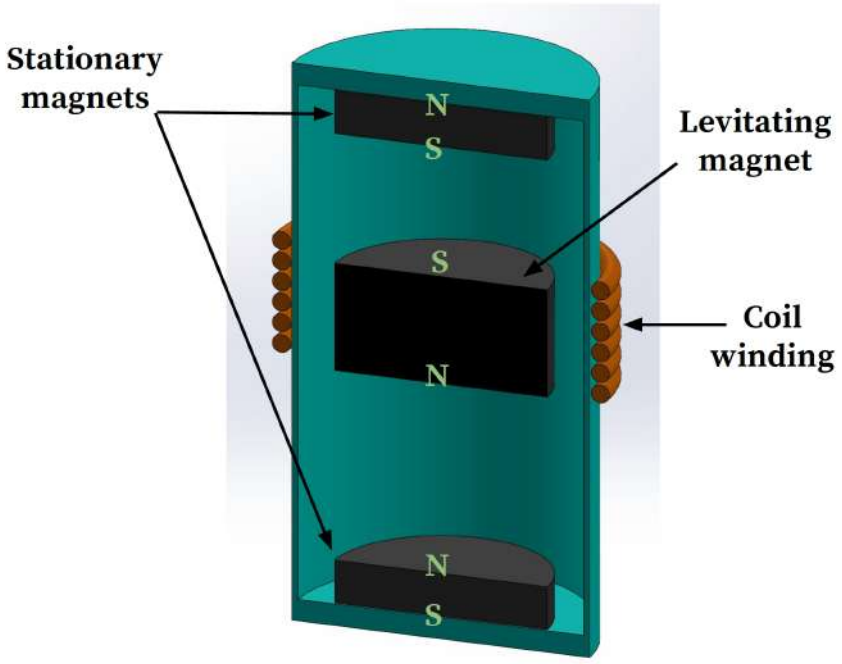

Figure 1.5: Cross-sectional view of a traditional magnetic-levitation based energy harvester.

Moreover, these magnetic spring based harvesters are characterized by their low output impedances. This ensures, relatively, large electric currents that can

meet the electric current threshold required to operate low-power sensors [24, 55]. Additionally, the mass of the levitated magnet in the harvester reduces its resonant frequency which further enables low frequency specialization [56]. This is especially important since most ambient vibration sources are rich with low frequencies [57, 58]. This configuration setup of magnets resolves the prevalent friction issue from magnets sliding against housing containers [59].

The need for a frictionless levitating magnet was the drive behind the work done by Palagummi and Yuan in making a mono-stable diamagnetic levitation energy harvester [59]. Their system consists of two diamagnetic plates (pyrolytic graphite), a center repelled floating magnet between the plates, and a top lifting magnet to stabilize the weight of the floating magnet. Power is generated through the coils attached to the top and bottom fixed diamagnetic plates that generated root mean square (rms) power of 1.72 μW under peak acceleration of 0.081 m/s^2 and frequency of 2.1 Hz. The system produces nonlinear hardening frequency response, i.e. a steep descent is observed in the curve once it reaches resonance. This is indicative of engagement of the system's nonlinearity from exploiting the magnetic levitation magnets setup configuration. Nonlinear frequency response, and tunable resonance adds leverage to the designed energy harvester. It allows compatibility of device function at varying excitation frequency environment.

Mann and Sims investigate the nonlinearity phenomenon in their mono-stable magnetic levitation based harvester and incorporate tunability of resonant frequency [13]. The system consists of two outer stationary magnets fixed on a threaded support, configured with an orientation to repel a center floating magnet. The threaded

support surface allows the user to vary the separation distance between the magnets, which allows control over the system's magnetic stiffness, thus allowing resonant frequency tunability. Their investigation of nonlinearities concludes that engagement of a system's nonlinear frequency response leads to relatively larger oscillations over a wider frequency spectrum. Larger oscillations can also be obtained from having a weaker magnetic flux in the floating magnet at the sides that are being repelled by the stationary magnets. Work done by Apo and Priya investigated the effect of reducing the magnetic flux of a center mono-stable floating magnet at its top and bottom sides where it gets repelled by outer top and bottom stationary magnets [14] as can be seen in Figure 1.6.

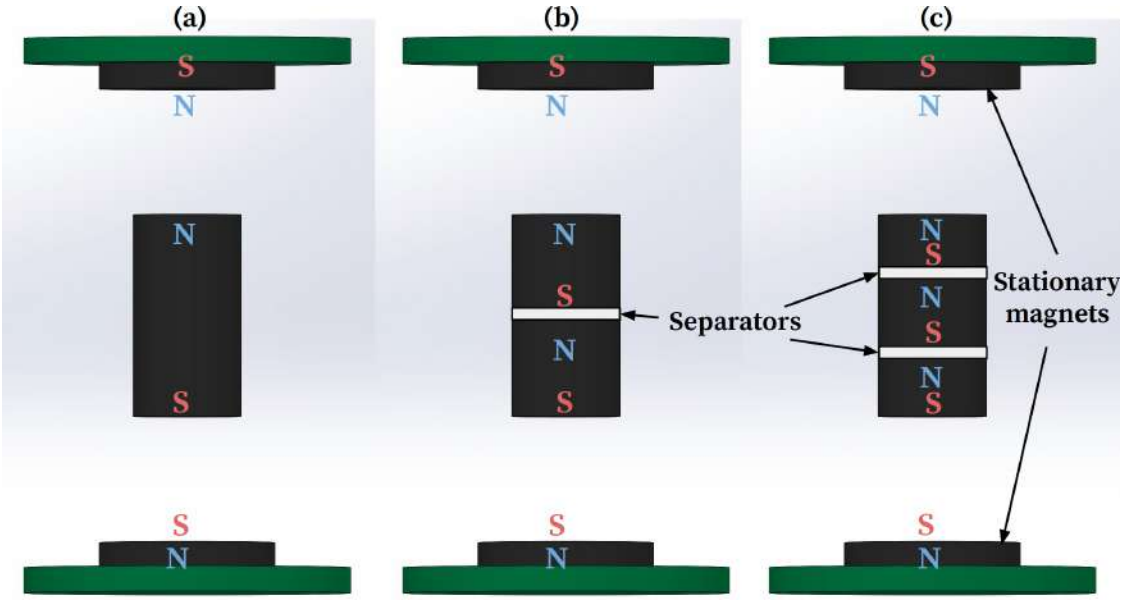

Figure 1.6: (a) Single levitating magnet, (b) two levitating magnets with one separator, (c) three moving magnets with two separators

The single levitating magnet would have a strong magnetic flux flowing from its poles compared to the two and three floating magnets in (b) and (c) [14]. However,

the two and three floating magnet configurations have stronger magnetic flux from the side compared to the single floating magnet; thus, more power can be generated from the coil windings around the floating magnets [14]. Furthermore, the weaker field from the top and bottom poles in the (b) and (c) configurations allow the magnet composite to float at larger oscillations since they have a weaker stiffness (k) value. This work had reported one of the highest power densities of 15.33 $mWcm^{-3}g^{-2}$ at 0.25 g and 13 Hz. The volume of the designed mono-stable harvester has considerable effect on its power density. Berdy et al. used block-shaped magnets to fabricate a magnetic spring based harvester [54]. The energy harvester produced 410 μW at 0.1 g and 6 Hz. They use block shaped magnets instead of cylindrical which allows for thinner device fabrication, where cylindrical magnets impose limits on the form factor [54].

Contrarily to the reviewed mono-stable work thus far, Gao et al. introduced a nonlinear multi-stable (quad-, tri-, bi-, and mono-stable) magnetic levitation-based energy harvesters. The quad-stable energy harvester depicted in Figure 1.7 generated a root-mean-square current of 80.15 mA and power of 440.98 mW, which was significantly higher than the other multi-stable harvesters they fabricated [24]. The levitating magnet had four stable points represented with dashed-lines. Chen et al. had incorporated a combination of linear and nonlinear springs in a modeled and fabricated multi degree-of-freedom (MDOF) electromagnetic energy harvester. The harvester utilized vertical linear springs and nonlinear magnetic springs based on magnetic levitation [60]. The fabricated prototype produced 78 mW at 0.5 g. Similarly, Abed et al. considered modal interactions and magnetic nonlinearities with numerical

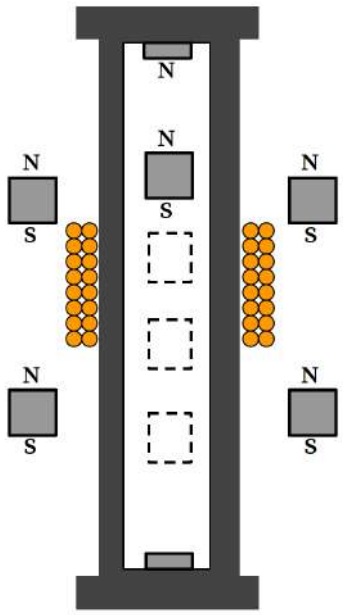

Figure 1.7: Quad-stable energy harvester schematic.

simulations showing an expected performance of 795 mW at 0.17 g for a three degree-of-freedom harvester [61].

1.4 Objective of the Work

This work explores a uniquely enhanced, magnetic spring-based energy harvester design that uses dual-mass MDOF, and a geometrically nonlinear FR4 planar spring. This enhancement will significantly improve power metrics over a traditional magnetic spring based energy harvester. The frequency responses of the traditional and enhanced design are modeled and the results are validated. The power measurements are taken for both designs and are compared to each other. Bandwidths comparison of traditional and enhanced design at different acceleration levels is formed. The normalized power is a power averaging method used to compensate for the change in volume and

acceleration values in both designs for a more accurate depiction of power output. This method is widely adopted in the field of energy harvesting and will be utilized in the assessment of both designs.

1.4.1 Structure of Thesis

In this work, prototypes of the Enhanced Energy Harvester (EEH) design are fabricated and their superiority over Traditional Energy Harvester (TEH) design is demonstrated. Three comparable EEH designs with various FR4 planar springs were fabricated along with one TEH design for direct analysis and comparison. The four harvesters were designed and manufactured using 3D printing and CNC tools which will be discussed in length in Chapter 2. Chapter 3 will carry out details of mathematical modeling for each energy harvester′s dynamical behavior which includes magnetic spring force displacement and frequency response. Static and dynamic characterization tests were conducted for all four harvesters. These tests will be discussed at length in Chapter 4. Merits of EEH design over traditional design and results from model and experiment are presented, the findings and outcomes from model and experiment are demonstrated in Chapter 5.

CHAPTER 2

DESIGN AND FABRICATION

2.1 Traditional Energy Harvester and Enhanced Energy Harvester Design

A schematic of the EEH introduced in this work compared with the TEH design is shown in Figure 2.1. In the TEH, the magnetic spring is made of two fixed (top and bottom) magnets and a middle levitated magnet. In the EEH design, the top magnet is freed and an FR4 mechanical spring is used to guide its motion. This yields varying distances between the levitated magnet and the top magnet which allow for improved conversion between the kinetic energy of the moving magnets and electric energy. That is, as the harvester is externally excited, energy in these oscillations is converted into kinetic energy of the moving magnet. The coil wrapped around the harvester casing is responsible for extracting electric energy from the kinetic energy of the moving levitated magnet. Additionally, the EEH design integrates a second top coil, which is used to harvest the kinetic energy from the top magnet that is guided by the FR4-spring. As will be demonstrated in this work, when stretched, the FR4 spring exhibits stiffness nonlinearity due to geometric stretching of the spring. This leads to improved performance and a venue for additional desired nonlinearity.

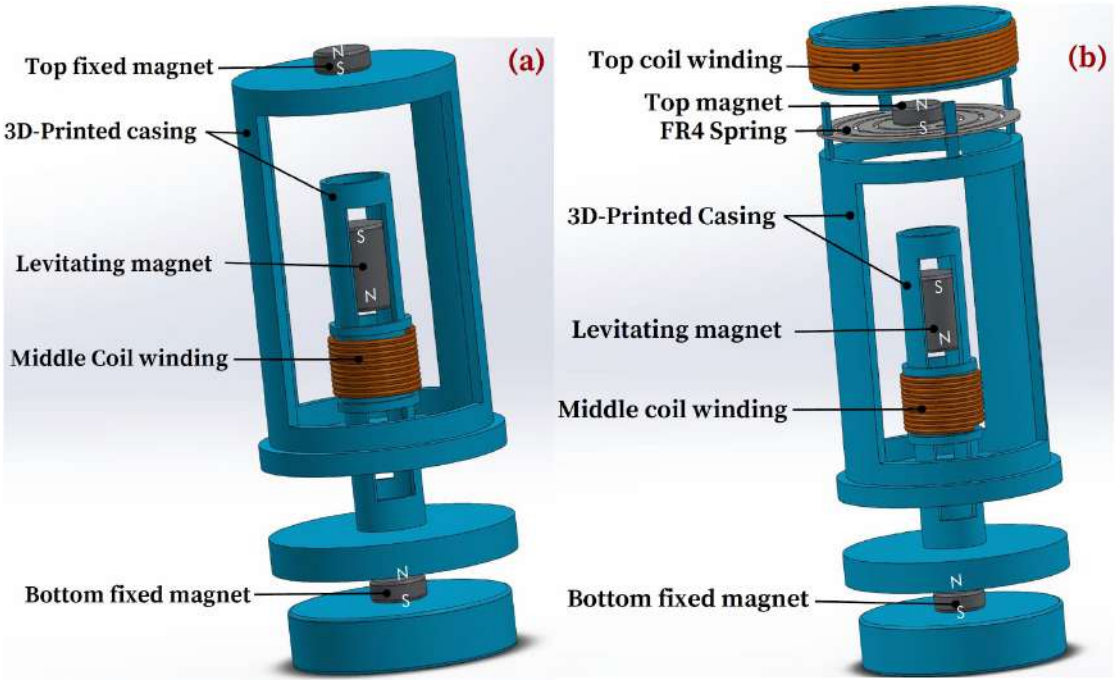

Figure 2.1: Exploded view schematic of enhanced versus traditional magnetic spring based energy harvesters: a) TEH and b) EEH.

The geometries of the harvesters adopted in this work are shown in Figure 2.2. In order to have a fair comparison, both TEH and EEH were built to have the same clearance in the levitating magnet tube, size of the magnets, the number of coil turns, and magnet distance to allow for matched comparison between their dynamic responses and performance metrics.

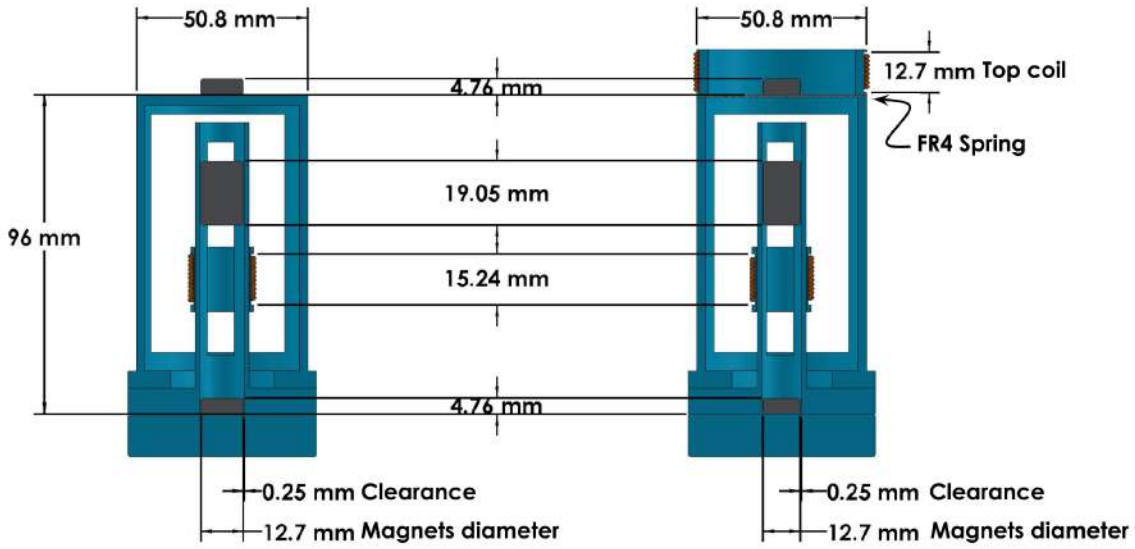

Figure 2.2: Cross-sectional view of design and geometry of the harvesters: a) TEH and b) EEH.

To fabricate both TEH and EEH, first, the casings of the harvesters were 3D printed using PLA filament. The filament type was essential in achieving a smooth surface for the magnets to travel in with minimal friction (3D universe 2.85 mm). The filaments were used for that purpose. For the TEH design, two neodymium iron boron (NdFeB) solid magnets were glued to the top and bottom of the harvester casing. A third magnet was carefully slid into the harvester and placed in a repulsive configuration with respect to the top and bottom fixed magnets as shown in Figure 9a. A copper wire was then placed around the equilibrium position of the levitated magnet. The wire was wound around a removable ring piece. This allowed for the coil to be removed when static (force displacement test) was conducted on the levitating magnet. The ring piece also accounted for uniformity of coil winding by having stoppers at both ends of the ring. The EEH design was fabricated in a similar fashion.

Upon assembly, the FR4 spring was anchored into the EEH casing, and the top magnet was glued to the center of the FR4 spring. This was then followed by winding the top coil around the casing as shown in Figure 2.1. Details of properties and dimensions for both of the assembled energy harvesters are given in Table 2.1. Figure 2.3 shows the fully fabricated and assembled TEH and EEH.

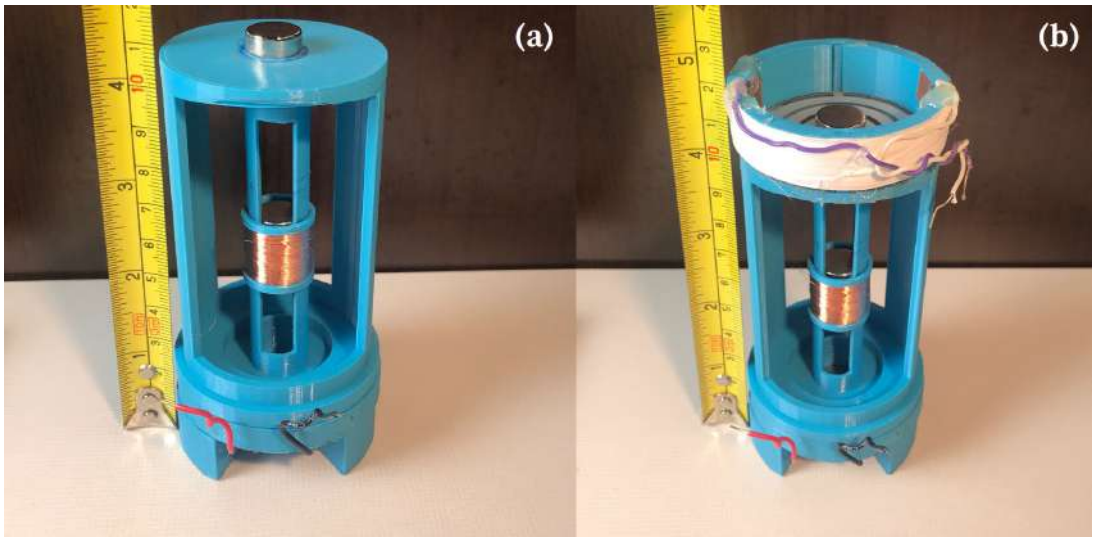

Figure 2.3: Fully fabricated and assembled harvesters: a) TEH and b) EEH.

Table 2.1 Material parameters and specifications

Coil		
Type	40 AWG enameled copper wire	
Diameter	Top: 50.8 mm	Middle: 17.4 mm
# turns	Top: 1500	Middle: 450
Resistance	Top: $\sim$ 890 ohm	Middle: $\sim$ 93 ohm
Magnets		
Material	NdFeB type N42	
Thickness	Top/Bottom: 4.76 mm	Middle: 19.05 mm
FR4 Spring		
Material	G10 FR4 fiberglass composite	
Thickness	0.64 mm	

2.2 FR4 Springs Design and Fabrication

The FR4 springs were first designed using SolidWorks computer aided design (CAD) software and then exported into a drawing exchange file (DXF). The file is then sent to Kern micro laser cutting machine (ker4824-ti100 micro) to cut the pattern onto FR4 sheets at 3.75 in/sec speed and 80% power. It is worthy of note that different laser settings (speed and power) will vary the stiffness of the cut springs. The intricate spring designs displayed in Figure 2.4 are geometry sensitive, so a slight shift in power or speed of cutting will result in deviation in the width of the 1.27 mm bridges. In this work, the three FR4 planer springs were fabricated and tested on the EEH. The FR4 springs were made of concentric rings that are connected through bridges as shown in Figure 2.4. Varying the number of concentric rings in each spring resulted in the three springs shown in Figure 2.4 (a-c) having three distinguished stiffness characteristics.

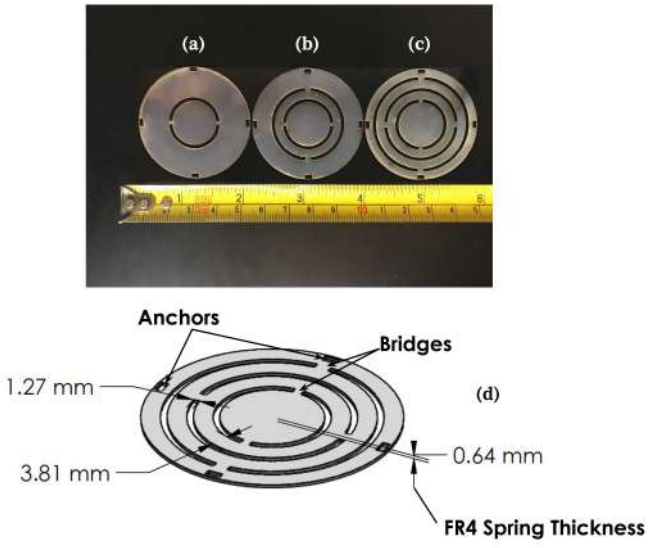

Figure 2.4: FR4 planar springs used in the EEH design: a) First FR4 spring design, b) Second FR4 spring design, c) Third FR4 spring design, and d) Dimensions and geometry.

CHAPTER 3

MODEL AND THEORY

In this section, mathematical models of the TEH and EEH are developed in order to understand and analyze the dynamic response of the harvesters. Since these harvesters represent coupled magnetic-mechanical nonlinear dynamic systems, first, the magnetic spring forces are formulated and then integrated into the equations of motion for both harvesters. Dynamic responses of the energy harvesters are obtained by solving their equations of motion numerically using the Runge-Kutta Method. This yields the displacement, velocity, and acceleration of the moving magnets. The solutions attained from these equations of motion are then used to obtain frequency responses and output voltages from the harvesters. Details are discussed next.

3.1 Formulation of Magnetic Forces

Appendix (A) contains the nomenclature used in this section. Figure 3.1 shows the schematic of the magnetic model of the harvesters. The magnetic field of a magnetic dipole inside the levitated magnet is expressed as [62]:

$$\boldsymbol{B}_d(\boldsymbol{r}) = \frac{\mu_0}{4\pi}\left[\frac{3\left(\mathfrak{m}\cdot(\boldsymbol{r}-\boldsymbol{r_d})\right)(\boldsymbol{r}-\boldsymbol{r_d})}{|\boldsymbol{r}-\boldsymbol{r_d}|^5} - \frac{\mathfrak{m}}{|\boldsymbol{r}-\boldsymbol{r_d}|^3}\right] \tag{3.1}$$

In Equation 3.1, $\boldsymbol{r_d}(\boldsymbol{x_d}, \boldsymbol{\theta_d}, \boldsymbol{\rho_d})$ is the vector position of the magnetic dipole inside the levitated magnet, and $\boldsymbol{r}(\boldsymbol{x}, \boldsymbol{\theta}, \boldsymbol{\rho})$ is the vector position of the point of evaluation in the cylindrical coordinate system shown in Figure 3.1a. Let the magnetic dipole $\mathfrak{m}$

point in the longitudinal direction, and the projection of this magnetic field along the longitudinal axis in a cylindrical coordinate system is expressed as:

$$B_d\left(x,\theta,\rho\right)=\frac{\mu_0 \mathbb{m}_1}{4\pi}\left[\frac{2(x-x_d)^2-\rho^2-{\rho_d}^2+2\rho\rho_d\cos(\theta-\theta_d)}{\left((x-x_d)^2+\rho^2+{\rho_d}^2-2\rho\rho_d\cos(\theta-\theta_d)\right)^{5/2}}\right] \tag{3.2}$$

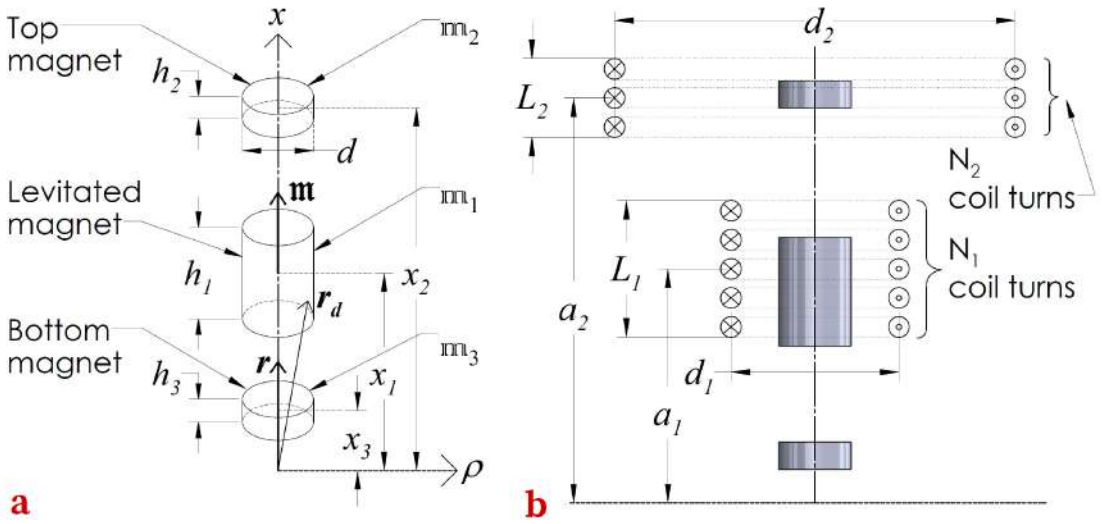

Figure 3.1: Magnetic model representation of the harvesters: a) Force derivation, and b) Voltage derivation.

Setting $\rho=0$, B_d becomes the dipoles magnetic field along the longitudinal axis and can be written as:

$$B_d|_{\rho=0}(x)=\frac{\mu_0 \mathbb{m}_1}{4\pi}\left[\frac{2(x-x_d)^2-{\rho_d}^2}{\left((x-x_d)^2+{\rho_d}^2\right)^{5/2}}\right] \tag{3.3}$$

The magnetic field of the levitated magnet along the longitudinal axis is the integration of B_d/V_1 over its volume and is given by:

$$\begin{aligned} B_1=&\int_{x_1-h_1/2}^{x_1+h_1/2}\int_0^{2\pi}\int_0^{d/2}\frac{B_d|_{\rho=0}(x)\,\rho_d}{V_1}d\rho_d d\theta_d dx_d \\ =&\frac{\mathbb{m}_1\mu_0}{2V_1}\left(\frac{h_1-2(x-x_1)}{\sqrt{d^2+(h_1-2(x-x_1))^2}}+\frac{h_1+2(x-x_1)}{\sqrt{d^2+(h_1+2(x-x_1))^2}}\right) \end{aligned} \tag{3.4}$$

Similar to 3.4, the magnetic field of the top and the bottom cylindrical magnets along the longitudinal axis is given by B_2 and B_3, respectively [2]:

$$B_2 = \frac{\mathbb{m}_2 \mu_0}{2} \left(\frac{h_2 - 2(x - x_2)}{\sqrt{d^2 + (h_2 - 2(x - x_2))^2}} + \frac{h_2 + 2(x - x_2)}{\sqrt{d^2 + (h_2 + 2(x - x_2))^2}} \right) \tag{3.5}$$

$$B_3 = \frac{\mathbb{m}_3 \mu_0}{2} \left(\frac{h_3 - 2(x - x_3)}{\sqrt{d^2 + (h_3 - 2(x - x_3))^2}} + \frac{h_3 + 2(x - x_3)}{\sqrt{d^2 + (h_3 + 2(x - x_3))^2}} \right) \tag{3.6}$$

Approximating the levitated magnet as one dipole, the total magnetic force acting on the levitated magnet is the gradient of the dot product between the surrounding magnet′s magnetic field and the levitated magnets dipole moment [62]. The axial component of this force is expressed as:

$$\begin{aligned} F_1^*(x_1) &= \frac{d}{dx}\left[(B_2 + B_3)\mathbb{m}_1\right] \\ &= \mathbb{m}_1 d^2 \mu_0 \left[\frac{\mathbb{m}_2}{V_2} \left(\frac{1}{\left(d^2 + [h_2 + 2(x_1 - x_2)]^2\right)^{3/2}} - \frac{1}{\left(d^2 + [h_2 - 2(x_1 - x_2)]^2\right)^{\frac{3}{2}}} \right.\right. \\ &\quad \left.\left. + \frac{\mathbb{m}_3}{V_3} \left(\frac{1}{\left(d^2 + [h_3 + 2(x_1 - x_3)]^2\right)^{\frac{3}{2}}} - \frac{1}{\left(d^2 + [h_3 - 2(x_1 - x_3)]^2\right)^{\frac{3}{2}}} \right) \right] \end{aligned} \tag{3.7}$$

Equation 3.7 can be improved by approximating the levitated magnet as $n = 3$ dipoles as shown in Figure 3.2. The improved expression of the total magnetic force acting on the levitated magnet is given by:

$$F_1(x_1) = \frac{1}{n} \sum_{i=1}^{n} F_1^* \left(x_1 - (i - \frac{n+1}{2} \frac{h_1}{n+1} \right), n = 3$$

$$= \frac{\mathbb{m}_1 d^2 \mu_0}{3} \sum_{i=1}^{3} \left\{ \frac{\mathbb{m}_2}{V_2} \left\{ \frac{1}{\left\{ d^2 + \left[h_2 + 2 \left(x_1 - x_2 - \frac{(i-2)h_1}{4} \right) \right]^2 \right\}^{\frac{3}{2}}} \right.\right.$$

$$
\left.
\begin{aligned}
&- \frac{1}{\left\{ d^2 + \left[h_2 - 2\left(x_1 - x_2 - \frac{(i-2)h_1}{4} \right) \right]^2 \right\}^{\frac{3}{2}}} \Bigg\} \\
&+ \frac{\mathbb{m}_3}{v_3} \left\{ \frac{1}{\left\{ d^2 + \left[h_3 + 2\left(x_1 - x_3 - \frac{(i-2)h_1}{4} \right) \right]^2 \right\}^{\frac{3}{2}}} \right. \\
&\left. - \frac{1}{\left\{ d^2 + \left[h_3 - 2\left(x_1 - x_3 - \frac{(i-2)h_1}{4} \right) \right]^2 \right\}^{\frac{3}{2}}} \right\} \Bigg\}
\end{aligned}
\tag{3.8}
$$

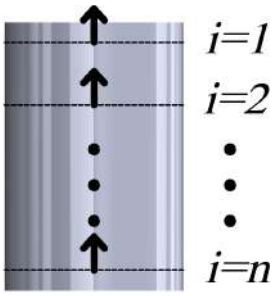

Figure 3.2: Multi-dipole approximation schematic of the levitated magnet.

Similar to Equation 3.7, the total magnetic force acting on the top cylindrical magnet is given by:

$$
\begin{aligned}
F_2(x_2) &= \frac{d}{dx}\left[(B_1 + B_3)\mathbb{m}_2 \right] \\
&= \mathbb{m}_2 d^2 \mu_0 \left[\frac{\mathbb{m}_1}{V_1} \left(\frac{1}{\left(d^2 + [h_1 + 2(x_2 - x_1)]^2 \right)^{3/2}} - \frac{1}{\left(d^2 + [h_1 - 2(x_2 - x_1)]^2 \right)^{3/2}} \right) \right. \\
&\left. + \frac{\mathbb{m}_3}{V_3} \left(\frac{1}{\left(d^2 + [h_3 + 2(x_2 - x_3)]^2 \right)^{3/2}} - \frac{1}{\left(d^2 + [h_3 - 2(x_2 - x_3)]^2 \right)^{3/2}} \right) \right]
\end{aligned}
\tag{3.9}
$$

The formulated magnetic spring forces are now integrated into the equations of motion of the harvesters as discussed next.

3.2 Equations of Motion

Figure 3.3 shows the mechanical model schematic of the harvester's free body diagrams. Assuming lateral motion of the moving magnets is negligible, the equation of motion of the levitated magnet in the traditional harvester is given by:

$$m_1\ddot{x}_1 + c_1(\dot{x}_1 - \dot{x}_3) + F_1 + m_1 g = 0 \tag{3.10}$$

Similarly, the equation of motion of the levitated magnet and the FR4 spring-guided top magnet in the enhanced harvester is described by a system of two equations:

$$\begin{cases} m_1\ddot{x}_1 + c_1(\dot{x}_1 - \dot{x}_3) + F_1 + (m_1)g & = 0 \\ m_2\ddot{x}_2 + c_2(\dot{x}_2 - \dot{x}_3) + F_2 + (m_2)g + F_s & = 0 \end{cases} \tag{3.11}$$

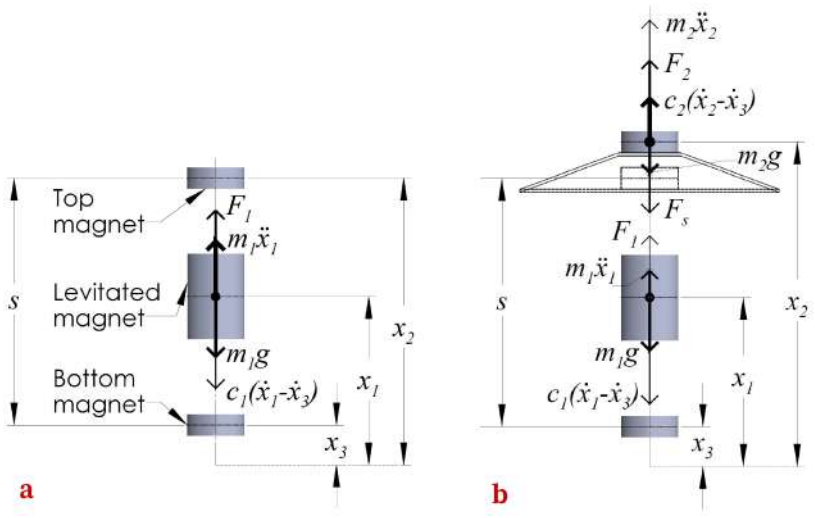

Figure 3.3: Mechanical model schematic of the harvesters: a) Free body diagram of the TEH and b) Free body diagram of the EEH.

Upon external base harmonic excitation, the position of the fixed bottom magnet x_3 is given by:

$$x_3 = \frac{A}{\omega^2} sin(\omega t) \tag{3.12}$$

In 3.11, the FR4 spring force, F_s, is represented as a third order polynomial function with only odd order terms [31]. The general form of the FR4 spring force is given as:

$$F_s = k_1(x_2 - x_3 - s) + k_3(x_2 - x_3 - s)^3 \tag{3.13}$$

For the three FR4 spring configurations shown in Figure 2.4 the set of terms (k_1, k_3) in Equation 3.13 becomes (k_1a, k_3a), (k_1b, k_3b), or (k_1c, k_3c), for the FR4-a, FR4-b, and FR4-c springs, respectively. The equations of motion describing the motion of the two masses, m_1 and m_2, are solved numerically to obtain their displacements and velocities. The attained solutions are then used to obtain the output voltages generated by the harvesters. Details are discussed next.

3.3 Formulation of Output Voltages from the Harvesters.

3.3.1 EEH

Based on Faraday′s Law, when the harvesters are externally excited, the kinetic energies of the moving magnets in the EEH are converted into electric energies as a result of change in magnetic fluxes across the surrounding coils. For the levitated magnet, setting $\rho_d = 0$, the expression of B_d in Equation 3.2 becomes the magnetic field of the levitated magnet approximated as a dipole placed on the axial line and is written as:

$$B_d|_{\rho=0}(x) = \frac{\mu_0 \mathbb{m}_1}{4\pi} \left[\frac{2(x - x_d)^2 - \rho^2}{\left((x - x)^2 + \rho^2\right)^{5/2}} \right] \tag{3.14}$$

The flux emanating from this field through all middle coil turns positioned around the levitated magnet is given by Figure 3.1:

$$\begin{aligned}\Phi_1^*(x_1) &= \frac{N_1}{L_1}\int_{x_3+a_1-L_1/2}^{x_3+a_1+L_1/2}\int_0^{2\pi}\int_0^{d_1/2}\left(B_d|_{\rho_d=0}\right)\rho d\rho d\theta dx \\ &= \frac{\mathbb{m}_1 N_1\mu_0}{2L_1}\left[\frac{L_1-2(x_1-x_3-a_1)}{\sqrt{\left(L_1-2(x_1-x_3-a_1)\right)^2+d_1^2}}\right. \\ &\qquad \left. + \frac{L_1+2(x_1-x_3-a_1)}{\sqrt{\left(L_1+2(x_1-x_3-a_1)\right)^2+d_1^2}}\right] \end{aligned} \tag{3.15}$$

Approximating the levitated magnet as 7 dipoles, the expression of flux in Equation 3.15 is improved and yields:

$$\begin{aligned}\Phi_1(x_1) = F_1(x_1) &= \frac{1}{n}\sum_{i=1}^{n}\Phi_1^*\left(x_1-(i-\frac{n+1}{2})\frac{h_1}{n+1}\right), n=7 \\ &= \frac{\mathbb{m}_1 N_1\mu_0}{14L_1}\sum_{i=1}^{7}\left[\frac{L_1-2(x_1-x_3-a_1-\frac{(i-4)h_1}{8})}{\sqrt{\left(L_1-2\left(x_1-x_3-a_1-\frac{(i-4)h_1}{8}\right)\right)^2+d_1^2}}\right. \\ &\qquad \left. + \frac{L_1+2(x_1-x_3-a_1-\frac{(i-4)h_1}{8})}{\sqrt{\left(L_1+2\left(x_1-x_3-a_1-\frac{(i-4)h_1}{8}\right)\right)^2+d_1^2}}\right] \end{aligned} \tag{3.16}$$

Similar to Equation 3.15, the flux emanating from the FR4 spring-guided top magnet approximated as a dipole through middle coil turns is given by:

$$\begin{aligned}\Phi_2(x_2) &= \frac{\mathbb{m}_2 N_1\mu_0}{2L_1}\left[\frac{L_1-2(x_2-x_3-a_1)}{\sqrt{\left(L_1-2\left(x_2-x_3-a_1\right)\right)^2+d_1^2}}\right. \\ &\qquad \left. + \frac{L_1+2(x_2-x_3-a_1)}{\sqrt{\left(L_2+2\left(x_1-x_3-a_1\right)\right)^2+d_1^2}}\right] \end{aligned} \tag{3.17}$$

The voltage generated in the middle coil due to the motion of the two moving magnets, i.e. the levitated magnet and the FR4 spring-guided top magnet in the EEH, is then given by [62]:

$$\epsilon_1 = -\frac{d(\Phi_1 + \Phi_2)}{dt}$$

$$\frac{N_1 d_1 \mu_0}{L_1}\left\{\frac{\mathbb{m}_1(\dot{x}_1 - \dot{x}_3)}{7}\sum_{i=1}^{7}\left\{\frac{1}{\left\{\left[L_1 - 2(x_1 - x_3 - a_1 - \frac{(i-4)h_1}{8})\right]^2 + d_1^2\right\}^{3/2}}\right.\right.$$

$$\left.\left. - \frac{1}{\left\{\left[L_1 + 2(x_1 - x_3 - a_1 - \frac{(i-4)h_1}{8})\right]^2 + d_1^2\right\}^{3/2}}\right\}$$

$$+ \mathbb{m}_2(\dot{x}_2 - \dot{x}_3)\left\{\frac{1}{\left\{[L_1 - 2(x_2 - x_3 - a_1)]^2 + d_1^2\right\}^{3/2}}\right.$$

$$\left. - \frac{1}{\left\{[L_1 + 2(x_2 - x_3 - a_1)]^2 + d_1^2\right\}^{3/2}}\right\}\Bigg\} \tag{3.18}$$

Similar to Equation 3.18, the voltage generated in the top coil turns due to the motion of the two moving magnets in the EEH is given by:

$$\epsilon_2 = \frac{N_2 d_2 \mu_0}{L_2}\left\{\frac{\mathbb{m}_2(\dot{x}_1 - \dot{x}_3)}{7}\sum_{i=1}^{7}\left\{\frac{1}{\left\{\left[L_2 - 2(x_1 - x_3 - a_2 - \frac{(i-4)h_1}{8})\right]^2 + d_2^2\right\}^{3/2}}\right.\right.$$

$$\left.\left. - \frac{1}{\left\{\left[L_2 + 2(x_1 - x_3 - a_2 - \frac{(i-4)h_1}{8})\right]^2 + d_1^2\right\}^{3/2}}\right\}$$

$$+ \mathbb{m}_2(\dot{x}_2 - \dot{x}_3)\left\{\frac{1}{\left\{[L_2 - 2(x_2 - x_3 - a_2)]^2 + d_2^2\right\}^{3/2}}\right.$$

$$\left. - \frac{1}{\left\{[L_2 + 2(x_2 - x_3 - a_2)]^2 + d_2^2\right\}^{3/2}}\right\}\Bigg\} \tag{3.19}$$

3.3.2 TEH

For the TEH design, the voltage generated from the middle coil is expressed in Equation 3.18. However, the term $(\dot{x}_2 - \dot{x}_3)$ vanishes since the top magnet and the bottom magnet are both fixed. The voltage $_1$ can be rewritten as:

$$\epsilon_1 = \frac{N_1 d_1 \mu_0 \mathbb{m}_1 (\dot{x}_1 - \dot{x}_3)}{7L_1} \sum_{i=1}^{7} \left\{ \frac{1}{\left\{ \left[L_1 - 2(x_1 - x_3 - a_1 - \frac{(i-4)h_1}{8}) \right]^2 + d_1^2 \right\}^{3/2}} - \frac{1}{\left\{ \left[L_1 + 2(x_1 - x_3 - a_1 - \frac{(i-4)h_1}{8}) \right]^2 + d_1^2 \right\}^{3/2}} \right\} \tag{3.20}$$

CHAPTER 4

EXPERIMENT

4.1 Overview

Experimental work was geared towards obtaining force-displacement curves and understanding the stiffness behavior of the harvesters. Additionally, the experimental work was focused on measuring the dynamic frequency responses and performance metrics of the harvesters.

4.2 Static Characterization

Figure 4.1 shows the experiment apparatus used to obtain magnetic forces, F_1 and F_2 given by Equation 3.8 and Equation 3.9, respectively, as well as measuring the restoring forces of the fabricated FR4 springs. A digital force sensor (SHIMPO FG-3006) fixed on a test stand (SHIMPO FGS-250W) was used to measure the magnetic force, while the displacement was monitored using a displacement sensor (KEYENCE IL-100). In order to measure the magnetic stiffness of the levitating magnet, a 3D printed force gauge attachment was utilized for the test. The windows on either side of the levitating magnet tube allowed for a nonferromagnetic rod to be placed on top of the levitating magnet after removing the coil ring. Pushing on the rod using the 3D printed attachment would result in force displacement variation that produced the experimental magnetic stiffness curve.

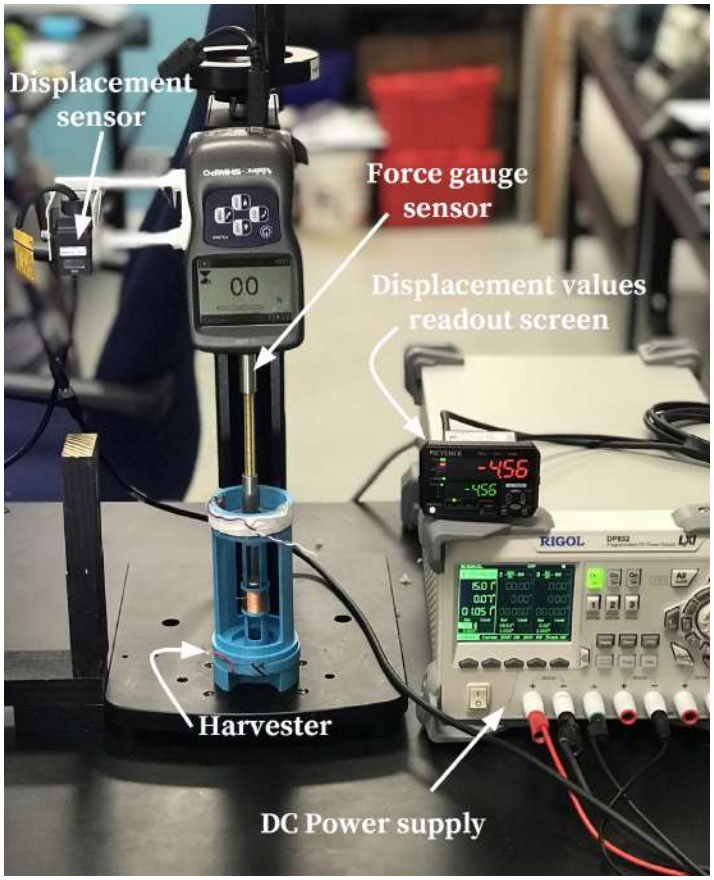

Figure 4.1: Experiment apparatus used for measuring restoring forces.

4.3 Dynamic Characterization

The windows on the levitating magnet tube also assist in the ring down experimental test. Ring down waveforms are used to find the mechanical damping coefficient for all four harvesters as seen in Figure 4.2. The waveforms were obtained by pushing down on the levitating magnet through the tube window using a nonferromagnetic rod and releasing the rod instantly for the magnet to oscillate freely.

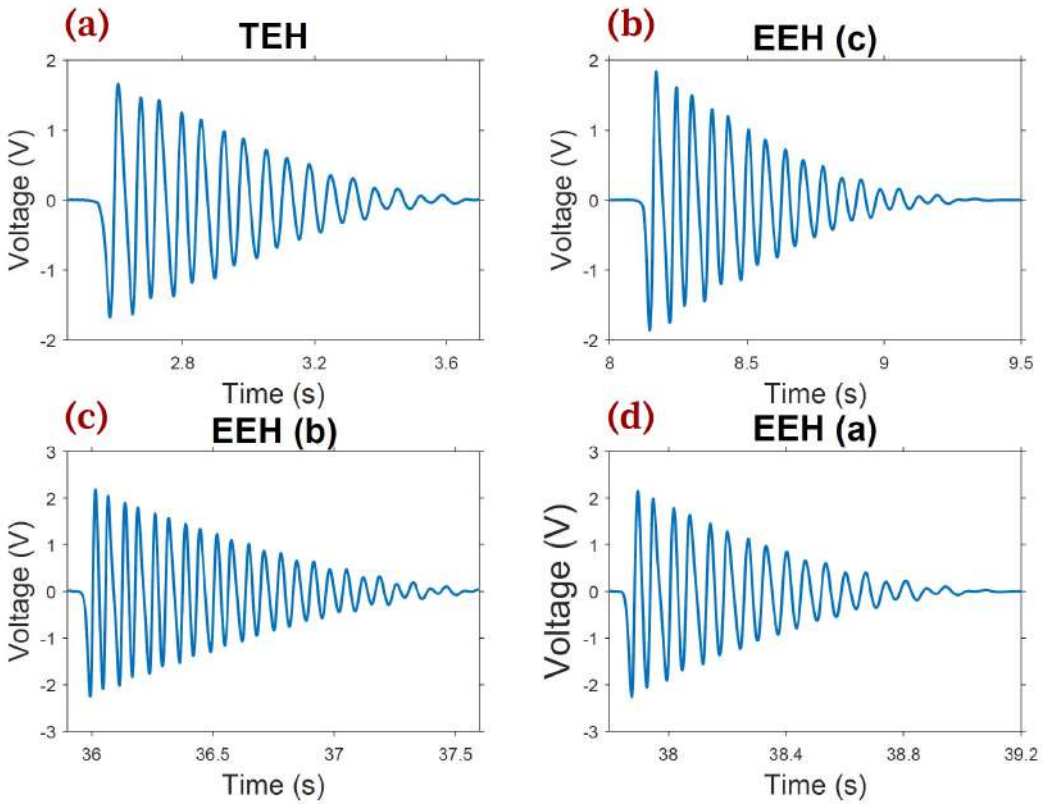

Figure 4.2: Ringdown waveforms for (a) TEH, (b) EEH-c, (c) EEH-b, and (d) EEH-d.

Figure 4.3 shows the experiment apparatus used to study the dynamic response of the harvesters. The setup consists of a shaker table (VT-500, SENTEK DYNAMICS), power amplifier (LA-800, SENTEK DYNAMICS), vibration controller (S81B-P02, SENTEK DYNAMICS), accelerometer (PCB333B30 model, PCB Piezotronics), data logger (NI myDAQ), and a PC. When performing the experiment, the harvester was securely mounted on a five-inch tall spacer to shield the effect of the magnetic field from the shaker table. The harvester response was measured at predetermined frequencies, i.e. $5 - 15$ $[Hz]$ and accelerations, i.e. 0.3 g, and 0.5 $g[m/s^2]$ using engineering data management software (EDM). The generated voltage from the harvester was measured and stored on the PC for later analysis.

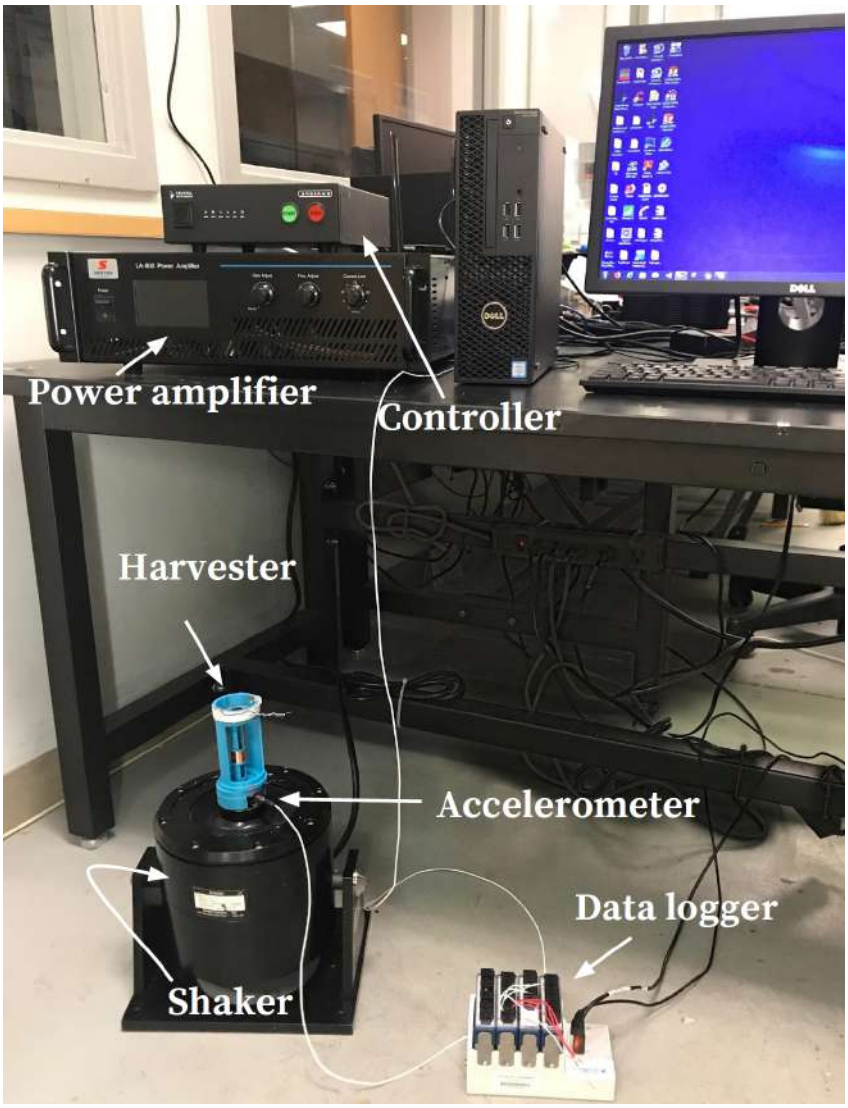

Figure 4.3: Experiment apparatus used for dynamic characterization of the fabricated harvesters.

The power measurements were conducted using the same dynamic testing setup with the addition of a resistance decade box model (RDB-10) that served as optimum load resistance source to the harvesters as seen in Figure 4.4.

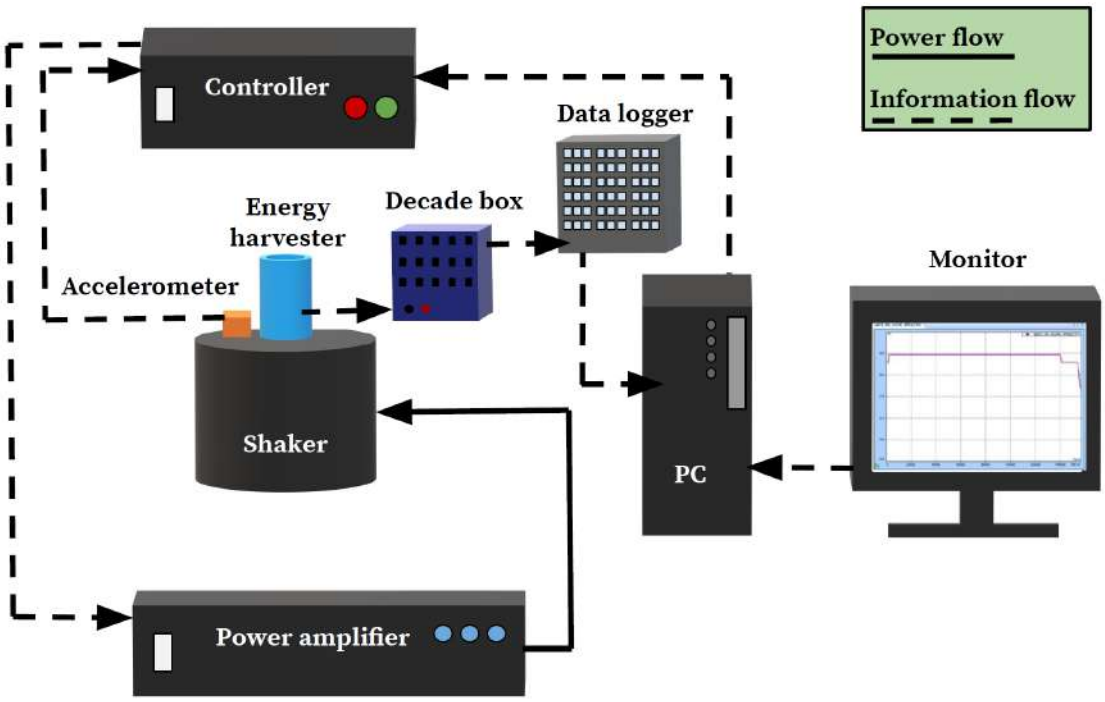

Figure 4.4: Schematic of experiment setup used for energy harvesters′ power measurements.

CHAPTER 5

RESULTS AND DISCUSSION

5.1 Overview

This chapter will present the measured magnetic stiffness of TEH and EEH compared to analytical and numerical model along with measured mechanical stiffness of the three FR4 springs. Open circuit voltage forward and backward frequency responses are compared with model predictions. The resulting power measurements at accelerations $(0.1, 0.3, 0.5)g$ are presented. Normalized power calculations are carried out and compared. The corresponding -3dB frequency bandwidth for the energy harvesters are analyzed.

5.2 Force Measurements and Model Validation

Measured magnetic force-displacement curves using the setup in Figure 4.1 are compared to those obtained using Equation 3.8 and Equation 3.9, respectively, in Figure 5.1 (a-b). Furthermore, two-dimensional (2D) axisymmetric models of magnetic forces F_1 and F_2 were developed using the AC/DC module in the COMSOL Multi-physics software. In these 2D models, magnets were represented by rectangles along the plane and all remaining edges of each magnet were magnetically insulated. A moving mesh function was used upon model simulation of the moving magnets as it oscillated between the fixed magnets. A parametric sweep is used to estimate the

magnetic restoring force as a result of the oscillatory motion of the moving magnets. Figure 5.1 reveals excellent agreement between COMSOL model simulations, analytical models given by Equation 3.8 and Equation 3.9, and measured magnetic forces. The nonlinear behavior of the magnetic forces is evident, especially at higher displacements.

The standard error associated with the force values of the experimental data are shown in Figure 5.2. Additionally, the FR4 springs are characterized using the setup shown in Figure 4.1. Figure 5.3 shows the measured force-displacement curves for the three FR4 springs fabricated in this work. Figure 5.3 shows that as the number of concentric rings increase, the FR4 spring becomes softer due to its ability to flex out more freely. Additionally, nonlinear stiffness manifests itself as the number of concentric rings decrease as shown in Figure 5.3.

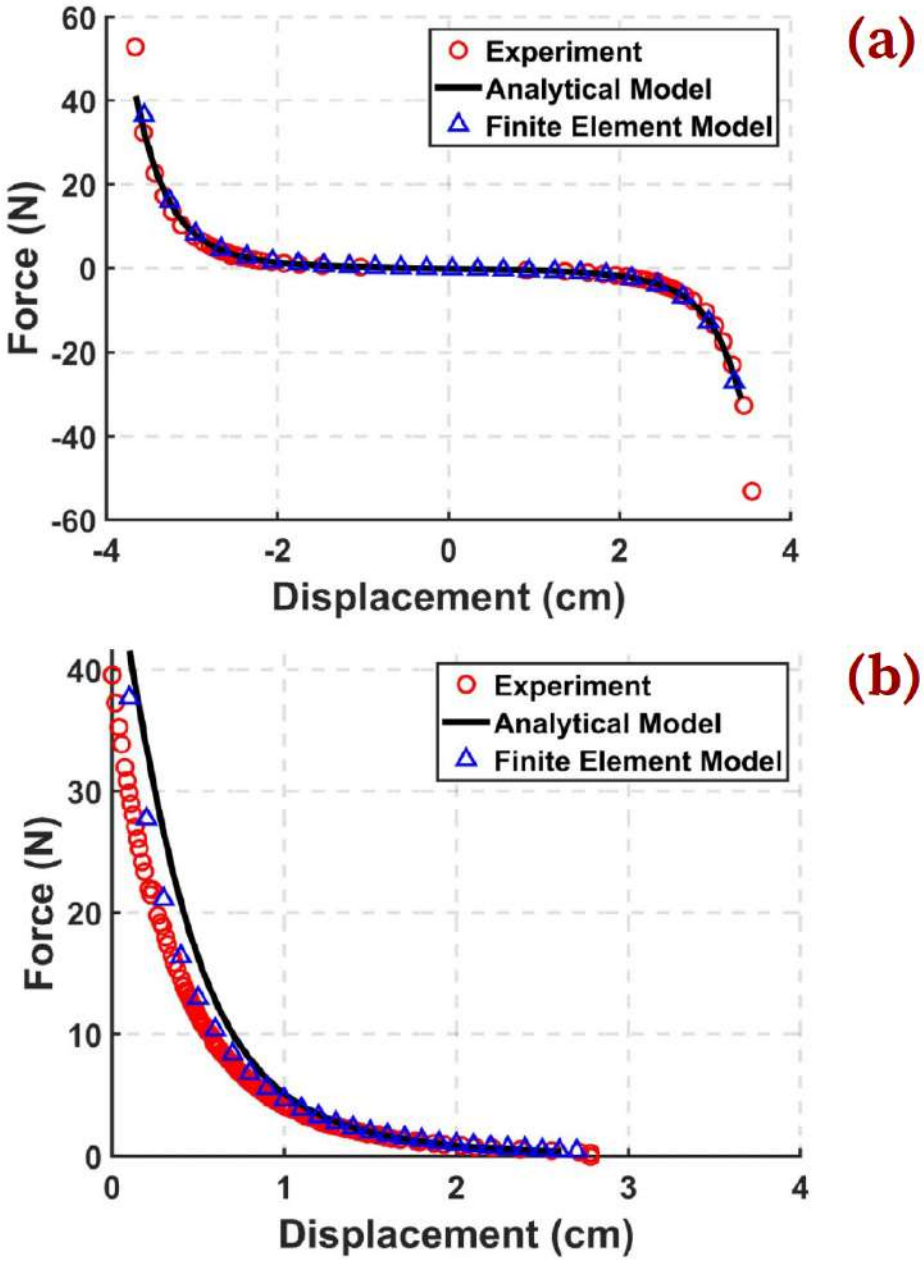

Figure 5.1: Measured and modeled magnetic spring forces: a) F1 acting on levitated magnet and b) F2 acting on top magnet.

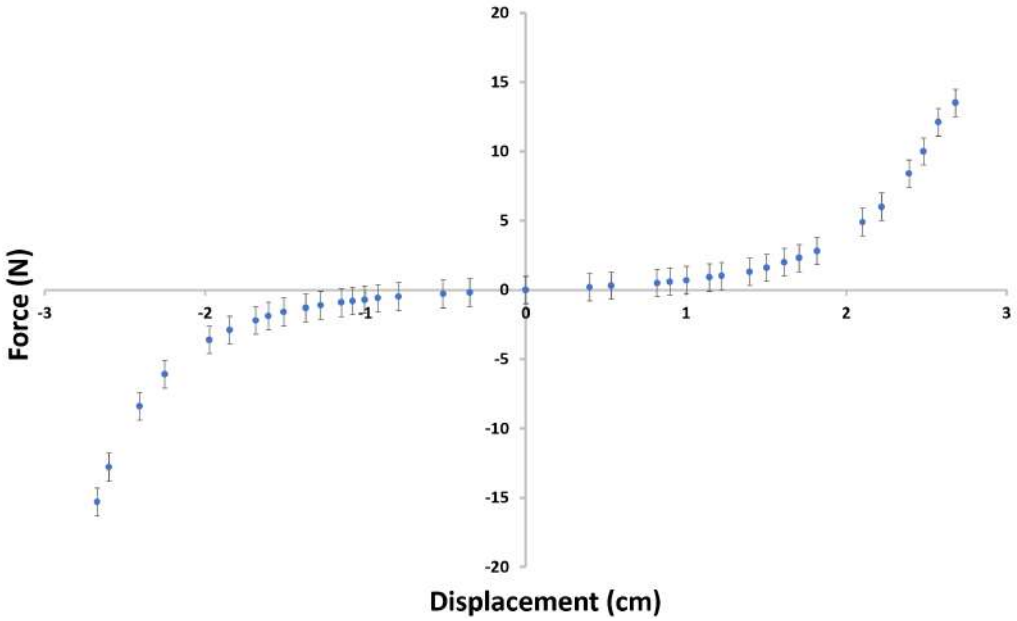

Figure 5.2: Measured magnetic spring force acting on the levitated magnet and the error associated with the force values.

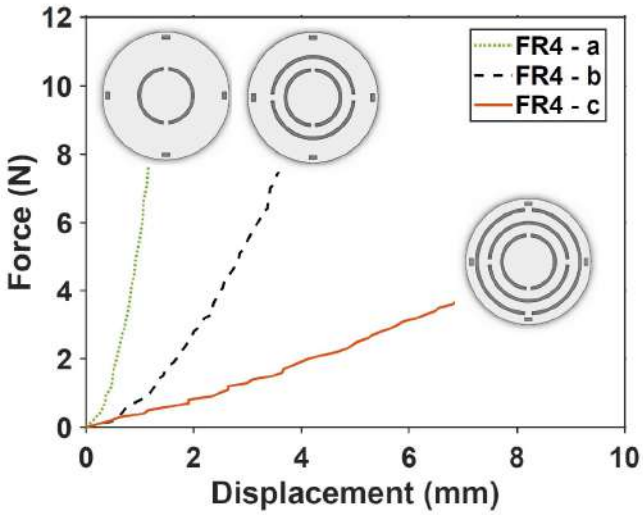

Figure 5.3: Measured restoring forces of the fabricated FR4-a, FR4-b, and FR4-c springs.

5.3 Open Circuit Voltage Frequency Response

Figure 5.4 shows the open circuit voltage frequency response using the setup in Figure 4.3 of the TEH during forward and backward sweeping obtained using experiment and model at 0.3 g and 0.5 $g[m/s^2]$, respectively. Similarly, Figures (5.5-5.7) compare the voltage frequency responses of the EEH using the three fabricated FR4 springs (FR4-a, FR4-b, and FR-c) at 0.3 g and 0.5 $g[m/s^2]$, respectively. Excellent agreement between model simulation and measured frequency response is evident for both TEH and EEH. Both experiment and model exhibit the nonlinear hardening effects in voltage frequency responses of both TEH and EEH harvesters. The non-resonant behavior of the harvesters due to nonlinear stiffness is evident. For instance, in Figures (5.4-5.7), comparing the frequency response of the levitated magnet at 0.3 g and 0.5 $g[m/s^2]$, one can notice that as the excitation level increased the voltage peak shifted towards the right side of the frequency response curve due to nonlinearity manifesting itself and hardening effects becoming more apparent.

Additionally, a sudden drop in the frequency response of the energy harvester is evident during forward sweeping. This is because the system moves from high to low stable points. This behavior is a characteristic of nonlinear Duffing oscillators and is commonly referred to as the frequency jump phenomena or saddle node point [31, 63]. The discontinuity occurs as a result of the coexistence of multiple energy states at the frequency branch [64]. During backward sweeping, the voltage peak occurres at a lower frequency. This hysteresis in forward and backward frequency response denotes the co-existence of multiple solutions [31, 63]. Similar observation can be made for the frequency response of the top magnet in the EEH Figures (5.5-5.7). That is,

the stiffness nonlinearity of the FR4 spring results in non-resonant behavior and a frequency jump in the frequency response of the top magnet as shown in Figures (5.5-5.7).

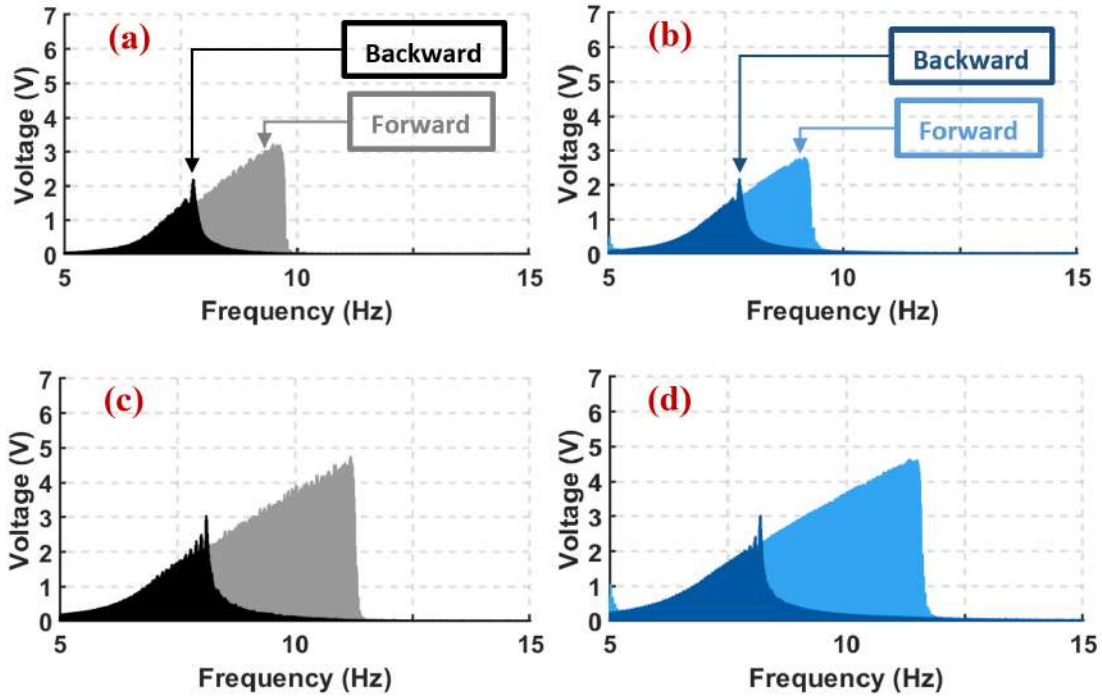

Figure 5.4: Forward and backward frequency response of TEH: a) Experiment at 0.3 $g[m/s^2]$, b) model at 0.3 $g[m/s^2]$, c) Experiment at 0.5 $g[m/s^2]$, and d) model at 0.5 $g[m/s^2]$. Experiment: Grey for forward and black for backward. Model: light blue for forward and dark blue for backward.

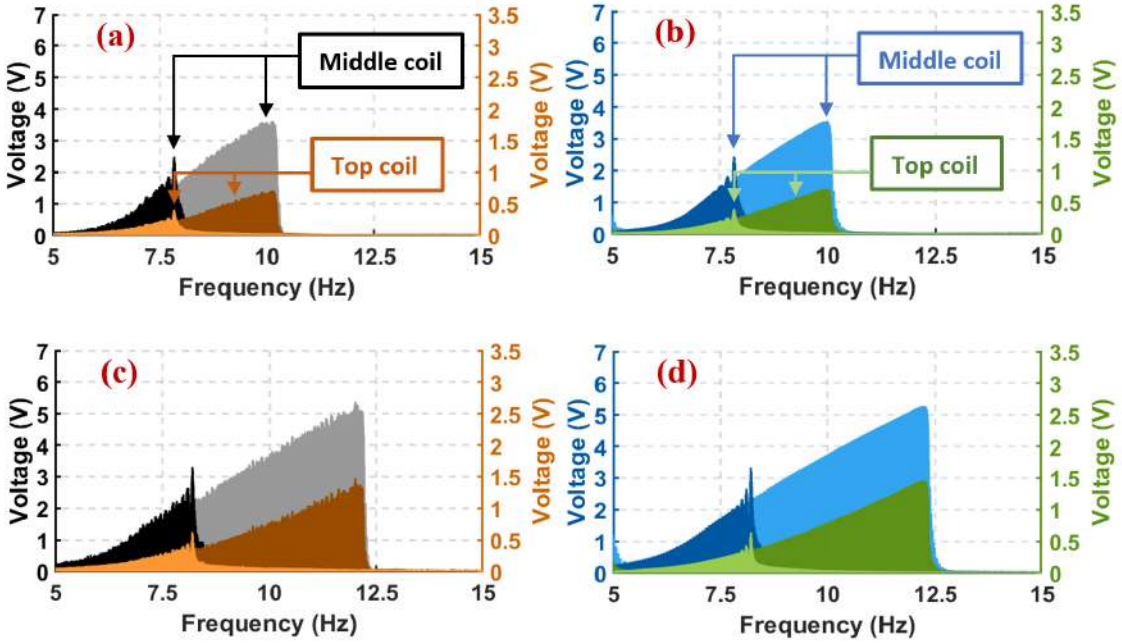

Figure 5.5: Forward and backward frequency response of TEH: a) Experiment at 0.3 $g[m/s^2]$, b) model at 0.3 $g[m/s^2]$, c) Experiment at 0.5 $g[m/s^2]$, and d) model at 0.5 $g[m/s^2]$. Experiment: Grey for forward and black for backward. Model: light blue for forward and dark blue for backward.

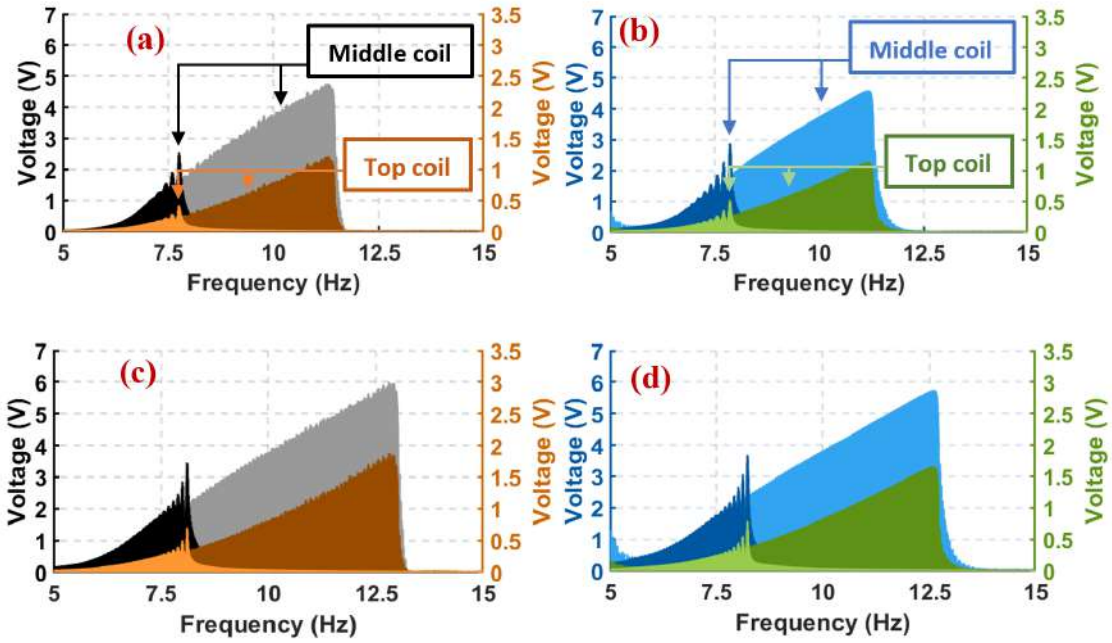

Figure 5.6: Forward and backward frequency response of EEH with FR4-a spring: a) Experiment at 0.3 $g[m/s^2]$, b) model at 0.3 $g[m/s^2]$, c) Experiment at 0.5 $g[m/s^2]$, and d) model at 0.5 $g[m/s^2]$. Experiment: Middle coil (grey for Forward and black for backward), Top coil (dark brown for forward and light brown for backward). Model: Middle coil (light blue for forward and dark blue for backward), Top coil (dark green for forward and light green for backward).

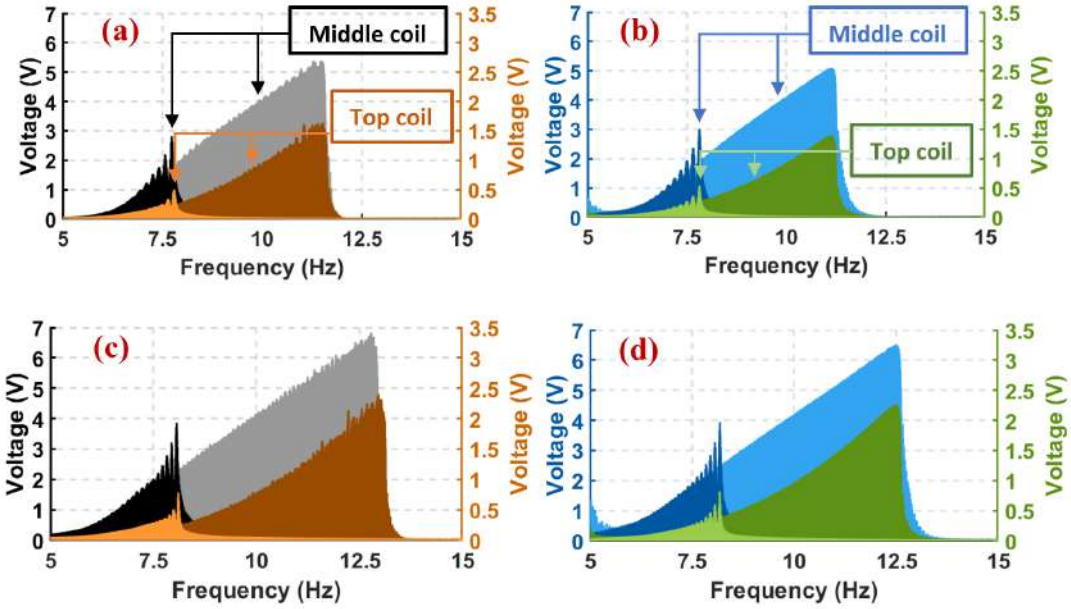

Figure 5.7: Forward and backward frequency response of EEH with FR4-c spring: a) Experiment at 0.3 $g[m/s^2]$, b) model at 0.3 $g[m/s^2]$, c) Experiment at 0.5 $g[m/s^2]$, and d) model at 0.5 $g[m/s^2]$. Experiment: Middle coil (grey for Forward and black for backward), Top coil (dark brown for forward and light brown for backward). Model: Middle coil (light blue for forward and dark blue for backward), Top coil (dark green for forward and light green for backward).

5.4 Power Measurements

Next, power metrics of the EEH design are compared to those of the TEH in Figures (5.8-5.9). Figure 5.8 shows the total power generated by the harvesters at three acceleration levels, i.e. 0.1 g, 0.3 g, and 0.5 $g[m/s^2]$. For these measurements, the optimum load resistance was first determined in order to maximize power transfer following the same procedure as in [31]. This was done by measuring the voltage produced by the energy harvesters across different load resistances using the setup in Figure 4.3. These optimum load resistance values were found to be approximately similar to the top and middle coil resistances shown in Table 2.1. This observation is similar to the one made by Mallick et al. [31] where maximum power transfer occurs

when the load resistance matches the internal resistance of the coil, i.e. impedance matching.

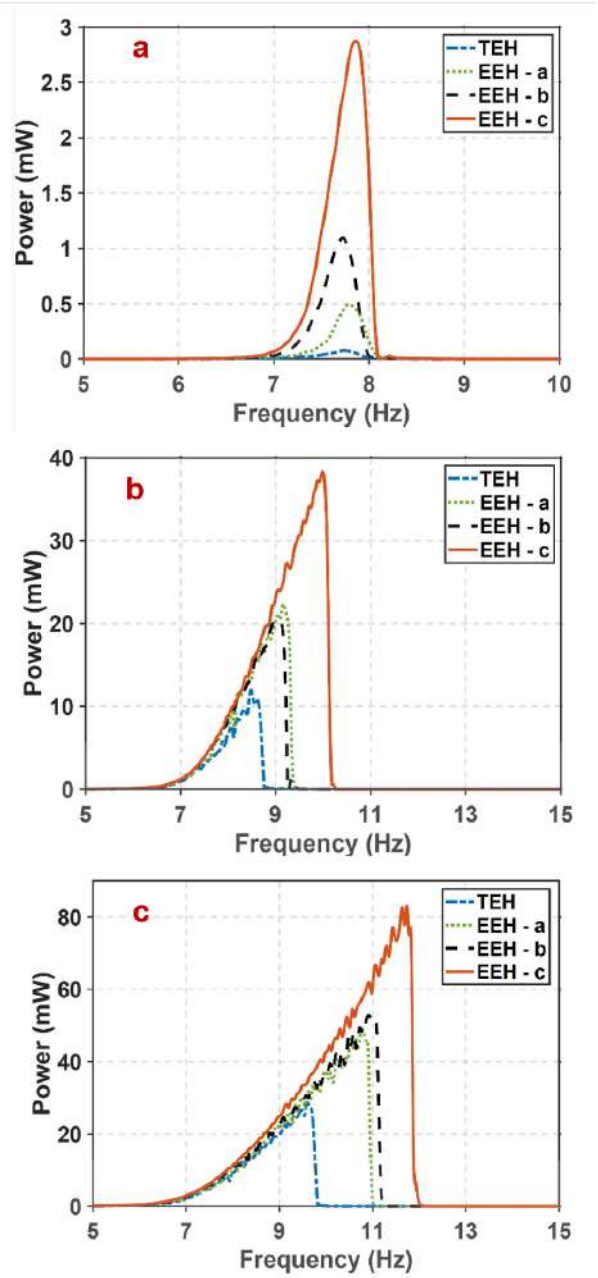

Figure 5.8: Power generated by the TEH and EEH (with FR4-a, FR4-b, FR4-c) at different acceleration levels: a) Power generation at 0.1 $g[m/s^2]$, b) Power generation at 0.3 $g[m/s^2]$, and c) Power generation at 0.5 $g[m/s^2]$.

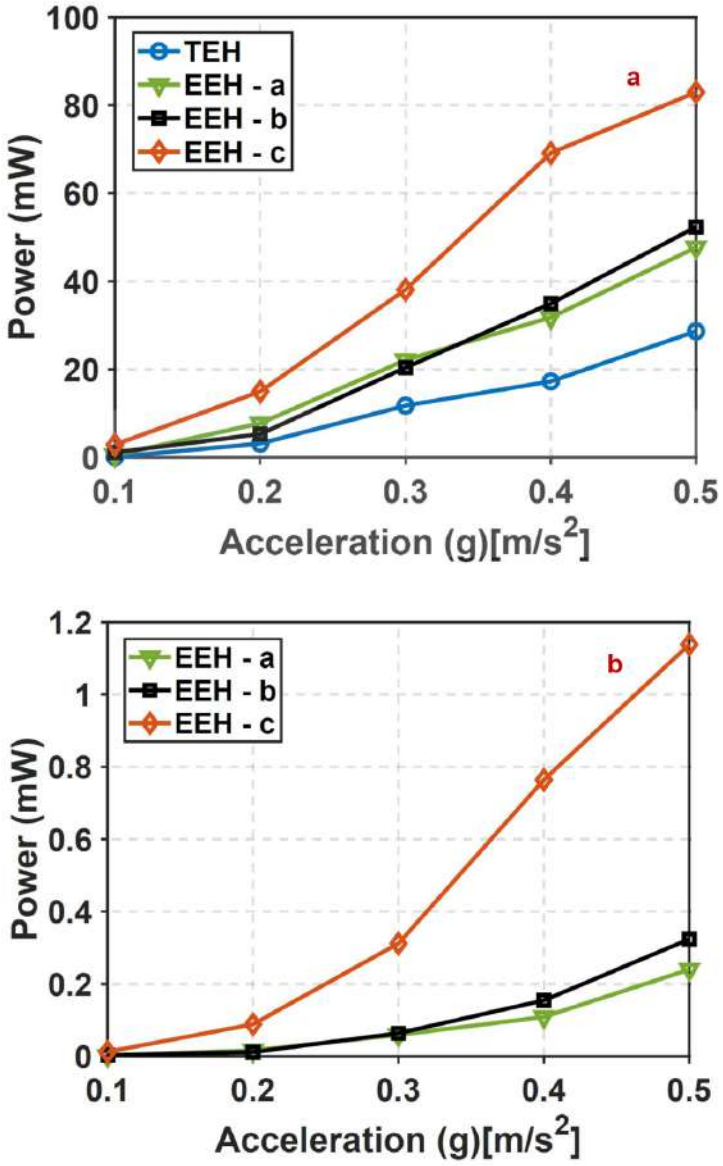

Figure 5.9: Comparison of power generation at different acceleration levels: a) Middle coil in the TEH and EEH, and b) Top coil in EEH.

The superiority of the EEH is evident in Figure 5.8 at all acceleration levels. Most notably, at lower acceleration level, i.e. 0.1 $g[m/s^2]$. For example, at 0.1 $g[m/s^2]$, the total peak power generated by the EEH with FR4-c spring is approximately 40 times higher than the power generated by the TEH. This significant increase in power generation in the EEH, compared to the TEH, is presumably due to freeing the top

magnet in the enhanced design, thus allowing the levitated magnet to move at higher velocity and with less constrained movement. Additionally, for a given FR4 spring design, the improvement in power generation by the EEH drops as the acceleration level increases. For example, for the EEH with FR4-c spring, the improvement in power generation drops to approximately a factor of 3 at 0.5 $g[m/s^2]$ (compared to a factor of 40 at 0.1 $g[m/s^2]$). This is likely because as the acceleration level increases, the FR4 spring is stretched to its maximum deflection and, therefore, resembles the traditional design where the movement of the top magnet is restrained.

Additionally, the FR4 spring-guided movement of the top magnet in the EEH contributes to the total power via power generation through the top coil. The amount of power portion generated in the top and middle coils is shown in Figure 5.9. It is evident that for the EEH design, most of the power is generated in the middle coil. This is expected since the size of the levitated magnet is much larger than the FR4 spring-guided top magnet. Also, the middle coil is placed closer to the levitated magnet compared to the position of the top coil relative to the FR4 spring-guided top magnet. These factors result in higher power generation in the middle coil compared to the top coil.

Figure 5.9 confirms the superiority of the soft (FR4-c) spring design over the other FR4 springs (FR4-a and FR4-b) tested in this work. While the EEH with the three implemented FR4 springs shows superior performance compared to the TEH, the EEH with the soft FR4 (FR4-c) spring yields the highest power generation at any acceleration level. For fixed acceleration, for instance 0.1 $g[m/s^2]$, the power ratio (defined as normalized power generated by the EEH over normalized power

generated by the TEH) decrease from approximately 40 to 15 and 6.6 for the EEH with FR4-c (Softest), FR4-b, and FR4-a (Stiffest) spring, respectively. This decay in power ratio is likely due to the gradual increase in stiffness of the three FR4 springs. Normalized power metrics are given in Table 5.1. Here, the power generated by the EEH and the TEH are normalized against their volumes and input acceleration levels. These normalized power metrics confirm the previous observations and emphasize the superiority of the EEH introduced in this work in comparison to the commonly used harvester, i.e. TEH.

Table 5.1 Normalized power comparison of TEH and EEH.

	Normalized Power [mW/cm3 g2]			
Base excitation (g)	**TEH**	**EEH-a**	**EEH-b**	**EEH-c**
0.1	0.034	0.226	0.503	1.35
0.2	0.36	1.13	0.64	1.75
0.3	0.607	1.14	1.018	1.92
0.4	0.500	0.92	1.035	1.97
0.5	0.529	0.891	0.974	1.55

5.5 Energy Harvester Bandwidth

Figure 5.10 compares the bandwidths of the TEH and the EEH at different acceleration levels. In Figure 5.10, the frequency bandwidth refers to the half-power bandwidth which corresponds to a $-3\ dB$ bandwidth. Results show that for both TEH and EEH, the bandwidth increases as the acceleration level is increased. This is due to the hardening nonlinearities of the magnetic spring and FR4 springs in TEH and EEH harvesters. At lower acceleration level, 0.1 g and 0.2 $g[m/s^2]$, the bandwidths of TEH and EEH harvesters are very narrow and, approximately, the

same, i.e. 0.4 $[Hz]$. As the acceleration level increases, the superiority of the EEH design over the TEH design becomes more evident. For example, at 0.3 g and 0.4 $g[m/s^2]$ the bandwidth of the EEH (with FR4-c spring) is improved by approximately 80% and 90%, respectively, compared to the TEH. This bandwidth superiority is likely due to the prominent nonlinearity introduced by the FR4 spring in the EEH design. At 0.5 $g[m/s^2]$ the bandwidths of all EEH plateau approximately at 60% level above the TEH due to the FR4 springs being stretched significantly.

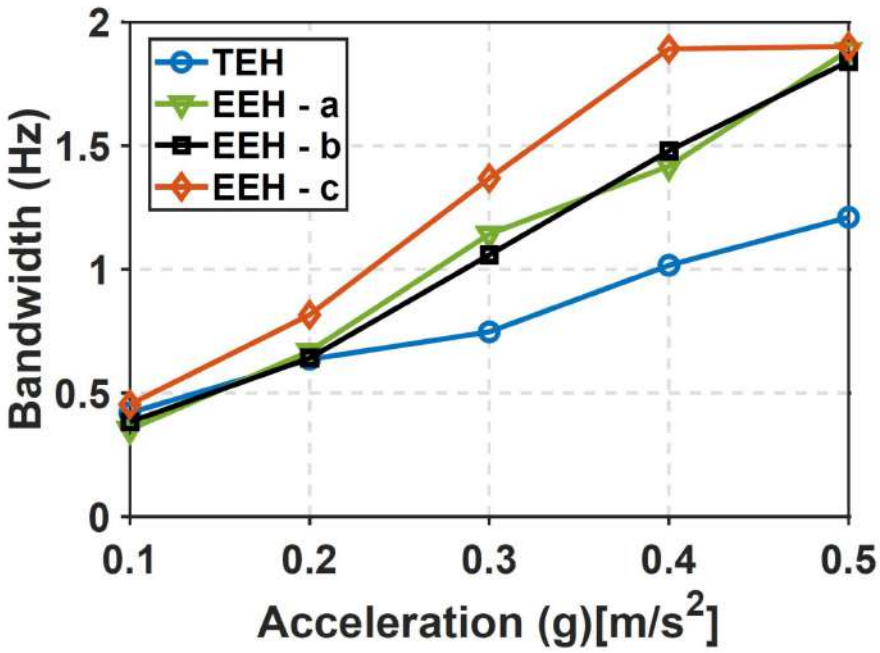

Figure 5.10: Comparison of bandwidths of traditional and enhanced harvesters at different acceleration levels.

CHAPTER 6

CONCLUSION AND FUTURE DIRECTION

In summary, a superior magnetic spring based nonlinear vibration energy harvester has been introduced in this work. Traditionally, a magnetic spring based harvester consists of a levitated magnet that is placed between two fixed top and bottom magnets. As the harvester is vibrated, the kinetic energy of the levitated magnet is converted into useful electric power using a coil placed around the casing of the harvester. Unlike commonly studied magnetic-spring based harvesters, the enhanced harvester introduced in this work frees the top fixed magnet and uses an FR4 spring to guide its motion. This allows for better energy conversion and improved performance of the harvester. Both experiment and model have been used to study the enhanced harvester design. Prototypes of the enhanced harvester have been fabricated and characterized. Specifically, three enhanced harvesters with three different FR4 spring dimensions have been fabricated and tested.

Moreover, for comparison, a traditional harvester with similar geometries and dimensions has been fabricated. Frequency response curves as well as performance metrics confirm the superiority of the enhanced design introduced in this work over the commonly studied harvester design. Results show excellent agreement between model and experiment. The figure of merits show that the presented enhanced design outperforms the commonly studied magnetic spring based vibration energy harvesters

under all conditions. Specifically, at low acceleration level, i.e. 0.1 $g[m/s^2]$, the power metrics of the EEH reach up to 1.35 $[mW/cm^3g^2]$ which is approximately 40 times higher than the TEH and both harvesters exhibit similar frequency bandwidths. As the acceleration level increases, i.e. 0.5 $g[m/s^2]$, power generation from the EEH is approximately 3 times the power generated by the TEH.

However, at this level of acceleration, the bandwidth of the EEH is approximately 60% higher than the TEH. For the purpose of studying the behavior of a spring-guided design, the FR4 material was chosen for spring material. However, the material is not ideal for practical application due to the fact that it is prone to plastic deformation at the smallest acceleration. This drawback of the material was mitigated by using disposable one time use FR4 springs for each test at every single acceleration. A future direction would be to find a higher quality material that can maintain elastic deformation under the above mentioned testing procedures. Realizing a high quality spring material along with miniaturization of the proposed design can allow practical use of the energy harvester in powering small sensors.

APPENDIX A

NOMENCLATURE

Table A.1 Nomenclature

Symbol	Definition	Value	Unit
a_1	The axial position of the center of the middle coil	4.39	cm
a_2	The axial position of the center of the top coil	9.68	cm
A	The acceleration amplitude of the bottom magnet and the shaker table	-	m_s^2
B_1	The scalar magnetic field on the axial line of the levitated magnet	-	T
B_2	The scalar magnetic field on the axial line of the top magnet	-	T
B_3	The scalar magnetic field on the axial line of the bottom magnet	-	T
B_d	The scalar magnetic field of a magnetic dipole inside the levitated magnet	-	T
$\mathbf{B_d}$	The magnetic vector field of a magnetic dipole inside the levitated magnet	-	T
c_1	The damping coefficient of the levitated magnet	-	Ns/m
c_2	The damping coefficient of the top magnet	-	Ns/m
d	The diameter of each magnet	12.7	mm
d_1	The diameter of the middle coil	17.4	mm
d_2	The diameter of the top coil	53.3	mm
F_1	The total magnetic force acting on the levitated magnet as 3 dipoles	-	N
F_1^*	The total magnetic force acting on the levitated magnet as 1 dipole	-	N

F_2	The total magnetic force acting on the top magnet	-	N
h_1	The height of the levitated magnet	19.1	mm
h_2	The height of the top magnet	4.76	mm
h_3	The height of the bottom magnet	4.76	mm
i	The summation index in multi-dipole approximations	-	1
k_1	The linear stiffness coefficient of a FR4 spring	-	N/m
k_3	The nonlinear stiffness coefficient of a FR4 spring	-	N/m
k_{1a}	The linear stiffness coefficient of the FR4-a spring	2,566	N/m
k_{3a}	The nonlinear stiffness coefficient of the FR4-a spring	2.963×10^9	N/m
k_{1b}	The linear stiffness coefficient of the FR4-b spring	1,002	N/m
k_{3b}	The nonlinear stiffness coefficient of the FR4-b spring	8.693×10^7	N/m
k_{1c}	The linear stiffness coefficient of the FR4-c spring	454.7	N/m
k_{3c}	The nonlinear stiffness coefficient of the FR4-c spring	1.414×10^6	N/m
L_1	The height of the middle coil	13.7	mm
L_2	The height of the top coil	12.7	mm
$\mathfrak{m}$	The dipole moment vector of the levitated magnet	-	$A \cdot m^2$
m_1	The mass of the levitated magnet	18.1	g

m_2	The mass of the top magnet	4.53	g
$\mathbb{m}_1$	The magnetic dipole moment of the levitated magnet	2.53	$A \cdot m^2$
$\mathbb{m}_2$	The magnetic dipole moment of the top magnet	-0.634	$A \cdot m^2$
$\mathbb{m}_3$	The magnetic dipole moment of the bottom magnet	-0.634	$A \cdot m^2$
n	Number of dipoles in multi-dipole approximations	-	1
N_1	The number of coil turn of the middle coil	450	1
N_2	The number of coil turn of the top coil	1,500	1
$\mathbf{r}$	The vector position of a point of evaluation	-	m
$\mathbf{r_d}$	The vector position of a magnetic dipole inside the levitated magnet	-	m
s	The distance between the equilibrium position of the top magnet and the position of the bottom magnet	96.012	mm
t	Time	-	s
V_1	Volume of the levitated magnet	2.41	cm^3
V_2	Volume of the top magnet	0.603	cm^3
V_3	Volume of the bottom magnet	0.603	cm^3
x	The axial position of a point of evaluation	-	m
x_1	The axial position of the center of the levitated magnet	-	m
$\dot{x}_1$	The velocity of the levitated magnet	-	m/s
$\ddot{x}_1$	The acceleration of the levitated magnet	-	m/s^2

x_2	The axial position of the center of the top magnet	-	m
$\dot{x}_2$	The velocity of the top magnet	-	m/s
$\ddot{x}_2$	The acceleration of the top magnet	-	m/s^2
x_3	The axial position of the center of the bottom magnet	-	m
$\dot{x_3}$	The velocity of the bottom magnet	-	m/s
x_d	The axial position of a dipole inside the levitated magnet	-	m
ϵ_1	The voltage generated in the middle coil	-	V
ϵ_2	The voltage generated in the top coil	-	V
θ	The azimuthal position of a point of evaluation	-	rad
θ_d	The azimuthal position of the dipole inside the levitated magnet	-	rad
μ_0	The permeability of free space	$4\pi \times 10^{-7}$	mkg/s^2A^2
ρ	The radial position of a point of evaluation	-	m
ρ_d	The radial position of the dipole inside the levitated magnet	-	m
Φ_1	The flux emanating from the levitated magnet approximated as 7 dipoles going through all coil turns of the middle coil	-	$V \cdot s$
Φ_1^*	The flux emanating from the levitated magnet approximated as 1 dipole going through all coil turns of the middle coil	-	$V \cdot s$
Φ_2	The flux emanating from the levitated magnet going through all coil turns of the middle coil	-	$V \cdot s$

ω	The angular frequency of vibration of the shaker table	-	rad

BIBLIOGRAPHY

[1] Peter Constantinou and Saibal Roy. A 3d printed electromagnetic nonlinear vibration energy harvester. *Smart Materials and Structures*, 25(9):095053, 2016.

[2] Mohammed F Daqaq, Ravindra Masana, Alper Erturk, and D Dane Quinn. On the role of nonlinearities in vibratory energy harvesting: a critical review and discussion. *Applied Mechanics Reviews*, 66(4):040801, 2014.

[3] Henry A Sodano, Daniel J Inman, and Gyuhae Park. A review of power harvesting from vibration using piezoelectric materials. *Shock and Vibration Digest*, 36(3):197–206, 2004.

[4] Shyamal Patel, Hyung Park, Paolo Bonato, Leighton Chan, and Mary Rodgers. A review of wearable sensors and systems with application in rehabilitation. *Journal of neuroengineering and rehabilitation*, 9(1):21, 2012.

[5] Chris Knight, Joshua Davidson, and Sam Behrens. Energy options for wireless sensor nodes. *Sensors*, 8(12):8037–8066, 2008.

[6] M Amin Karami and Daniel J Inman. Powering pacemakers from heartbeat vibrations using linear and nonlinear energy harvesters. *Applied Physics Letters*, 100(4):042901, 2012.

[7] Gerbert J Renzenbrink and Maarten J Ijzerman. Percutaneous neuromuscular electrical stimulation (p-nmes) for treating shoulder pain in chronic hemiplegia. effects on shoulder pain and quality of life. *Clinical rehabilitation*, 18(4):359–365, 2004.

[8] Niell G Elvin, Nizar Lajnef, and Alex A Elvin. Feasibility of structural monitoring with vibration powered sensors. *Smart materials and structures*, 15(4):977, 2006.

[9] Shad Roundy. On the effectiveness of vibration-based energy harvesting. *Journal of intelligent material systems and structures*, 16(10):809–823, 2005.

[10] Shad Roundy, Paul Kenneth Wright, and Jan M Rabaey. Energy scavenging for wireless sensor networks. In *Norwell*, pages 45–47. Springer, 2003.

[11] M Amin Karami and Daniel J Inman. Electromechanical modeling of the low-frequency zigzag micro-energy harvester. *Journal of Intelligent Material Systems and Structures*, 22(3):271–282, 2011.

[12] Sebastien Boisseau, Ghislain Despesse, and Bouhadjar Ahmed Seddik. Nonlinear h-shaped springs to improve efficiency of vibration energy harvesters. *Journal of*

Applied Mechanics, 80(6):061013, 2013.

[13] BP Mann and ND Sims. Energy harvesting from the nonlinear oscillations of magnetic levitation. *Journal of Sound and Vibration*, 319(1-2):515–530, 2009.

[14] Daniel J Apo and Shashank Priya. High power density levitation-induced vibration energy harvester. *Energy Harvesting and Systems*, 1(1-2):79–88, 2014.

[15] Christopher Lee, David Stamp, Nitin R Kapania, and José Oscar Mur-Miranda. Harvesting vibration energy using nonlinear oscillations of an electromagnetic inductor. In *Energy Harvesting and Storage: Materials, Devices, and Applications*, volume 7683, page 76830Y. International Society for Optics and Photonics, 2010.

[16] S P Beeby, M J Tudor, and NM White. Energy harvesting vibration sources for microsystems applications. *Measurement science and technology*, 17(12):R175, 2006.

[17] Maryam Ghandchi Tehrani and Stephen J Elliott. Extending the dynamic range of an energy harvester using nonlinear damping. *Journal of Sound and Vibration*, 333(3):623–629, 2014.

[18] Ph Krauchi, PA Wager, Martin Eugster, Günter Grossmann, and L Hilty. End-of-life impacts of pervasive computing. *IEEE Technology and Society Magazine*, 24(1):45–53, 2005.

[19] Innovation Union. Communication from the commission to the european parliament, the council, the european economic and social committee and the committee of the regions. *Brussels. http://ww. w. xploit-eu. com/pdfs/Europe*, 202020:20, 2014.

[20] Miao Yun and Bu Yuxin. Research on the architecture and key technology of internet of things (iot) applied on smart grid. In *2010 International Conference on Advances in Energy Engineering*, pages 69–72. IEEE, 2010.

[21] Naser Hossein Motlagh, Tarik Taleb, and Osama Arouk. Low-altitude unmanned aerial vehicles-based internet of things services: Comprehensive survey and future perspectives. *IEEE Internet of Things Journal*, 3(6):899–922, 2016.

[22] In Lee and Kyoochun Lee. The internet of things (iot): Applications, investments, and challenges for enterprises. *Business Horizons*, 58(4):431–440, 2015.

[23] Shashank Priya and Daniel J Inman. *Energy harvesting technologies*, volume 21. Springer, 2009.

[24] Mingyuan Gao, Yuan Wang, Yifeng Wang, and Ping Wang. Experimental investigation of non-linear multi-stable electromagnetic-induction energy harvesting mechanism by magnetic levitation oscillation. *Applied Energy*, 220:856–875, 2018.

[25] L Siegele. A sea of sensors: Special report: smart systems. *The Economist*, pages 5–6, 2010.

[26] Abhiman Hande, Todd Polk, William Walker, and Dinesh Bhatia. Indoor solar energy harvesting for sensor network router nodes. *Microprocessors and Microsystems*, 31(6):420–432, 2007.

[27] Alper Erturk and Daniel J Inman. An experimentally validated bimorph cantilever model for piezoelectric energy harvesting from base excitations. *Smart materials and structures*, 18(2):025009, 2009.

[28] JD Hobeck and DJ Inman. Artificial piezoelectric grass for energy harvesting from turbulence-induced vibration. *Smart Materials and Structures*, 21(10):105024, 2012.

[29] Paul D Mitcheson, Peng Miao, Bernard H Stark, EM Yeatman, AS Holmes, and TC Green. Mems electrostatic micropower generator for low frequency operation. *Sensors and Actuators A: Physical*, 115(2-3):523–529, 2004.

[30] Nenad Miljkovic, Daniel J Preston, Ryan Enright, and Evelyn N Wang. Jumping-droplet electrostatic energy harvesting. *Applied Physics Letters*, 105(1):013111, 2014.

[31] Dhiman Mallick, Andreas Amann, and Saibal Roy. A nonlinear stretching based electromagnetic energy harvester on fr4 for wideband operation. *Smart Materials and Structures*, 24(1):015013, 2014.

[32] Steve P Beeby, RN Torah, MJ Tudor, P Glynne-Jones, T O'donnell, CR Saha, and S Roy. A micro electromagnetic generator for vibration energy harvesting. *Journal of Micromechanics and microengineering*, 17(7):1257, 2007.

[33] S Boisseau, G Despesse, and B Ahmed Seddik. Electrostatic conversion for vibration energy harvesting. *arXiv preprint arXiv:1210.5191*, 2012.

[34] Mohd Fauzi Bin Ab Rahman and Swee Leong Kok. Investigation of useful ambient vibration sources for the application of energy harvesting. In *2011 IEEE Student Conference on Research and Development*, pages 391–396. IEEE, 2011.

[35] Shashank Priya. Advances in energy harvesting using low profile piezoelectric transducers. *Journal of electroceramics*, 19(1):167–184, 2007.

[36] CB Williams and Rob B Yates. Analysis of a micro-electric generator for microsystems. *sensors and actuators A: Physical*, 52(1-3):8–11, 1996.

[37] A Cammarano, SA Neild, SG Burrow, DJ Wagg, and DJ Inman. Optimum resistive loads for vibration-based electromagnetic energy harvesters with a stiffening nonlinearity. *Journal of Intelligent Material Systems and Structures*, 25(14):1757–1770, 2014.

[38] Alper Erturk and Daniel J Inman. *Piezoelectric energy harvesting*. John Wiley & Sons, 2011.

[39] Hyun-Cheol Song, Prashant Kumar, Deepam Maurya, Min-Gyu Kang, William T

Reynolds, Dae-Yong Jeong, Chong-Yun Kang, and Shashank Priya. Ultra-low resonant piezoelectric mems energy harvester with high power density. *Journal of Microelectromechanical Systems*, 26(6):1226–1234, 2017.

[40] Rita T Aljadiri, Luay Y Taha, and Paul Ivey. Electrostatic energy harvesting systems: a better understanding of their sustainability. *Journal of Clean Energy Technologies*, 5(5):409–416, 2017.

[41] Loreto Mateu and Francesc Moll. Review of energy harvesting techniques and applications for microelectronics (keynote address). In *VLSI Circuits and Systems II*, volume 5837, pages 359–374. International Society for Optics and Photonics, 2005.

[42] P Miao, AS Holmes, EM Yeatman, TC Green, and PD Mitcheson. Micro-machined variable capacitors for power generation.

[43] Markus Zahn. Magnetic fluid and nanoparticle applications to nanotechnology. *Journal of nanoparticle research*, 3(1):73–78, 2001.

[44] Wen-Ming Zhang, Han Yan, Zhi-Ke Peng, and Guang Meng. Electrostatic pull-in instability in mems/nems: A review. *Sensors and Actuators A: Physical*, 214:187–218, 2014.

[45] Matthew NO Sadiku. *Elements of electromagnetics*. Oxford university press, 2014.

[46] Zhiyi Wu, Jianhong Tang, Xin Zhang, and Zhicheng Yu. An energy harvesting bracelet. *Applied Physics Letters*, 111(1):013903, 2017.

[47] Ting Quan, Xue Wang, Zhong Lin Wang, and Ya Yang. Hybridized electromagnetic–triboelectric nanogenerator for a self-powered electronic watch. *ACS nano*, 9(12):12301–12310, 2015.

[48] Igor A Khovanov and Natasha A Khovanova. Frequency response of an energy harvester to harmonic noise: Towards stochastic frequency response of nonlinear systems. In *2017 International Conference on Noise and Fluctuations (ICNF)*, pages 1–4. IEEE, 2017.

[49] Abdullah Nammari, Logan Caskey, Johnny Negrete, and Hamzeh Bardaweel. Fabrication and characterization of non-resonant magneto-mechanical low-frequency vibration energy harvester. *Mechanical Systems and Signal Processing*, 102:298–311, 2018.

[50] Abdullah Nammari, Seth Doughty, Dustin Savage, Leland Weiss, Arun Jaganathan, and Hamzeh Bardaweel. Design and analysis of a small-scale magnetically levitated energy harvester utilizing oblique mechanical springs. *Microsystem Technologies*, 23(10):4645–4657, 2017.

[51] SM Mahdi Mofidian and Hamzeh Bardaweel. A dual-purpose vibration isolator

energy harvester: Experiment and model. *Mechanical Systems and Signal Processing*, 118:360–376, 2019.

[52] Hieu Nguyen and Hamzeh Bardaweel. Multi-stable magnetic spring-based energy harvester subject to harmonic excitation: Comparative study and experimental evaluation. In *ASME 2018 International Mechanical Engineering Congress and Exposition*, pages V04BT06A038–V04BT06A038. American Society of Mechanical Engineers, 2018.

[53] Mohammed F Daqaq. On intentional introduction of stiffness nonlinearities for energy harvesting under white gaussian excitations. *Nonlinear Dynamics*, 69(3):1063–1079, 2012.

[54] DF Berdy, DJ Valentino, and D Peroulis. Design and optimization of a magnetically sprung block magnet vibration energy harvester. *Sensors and actuators A: Physical*, 218:69–79, 2014.

[55] Arian Rahimi, Özge Zorlu, Ali Muhtaroglu, and Haluk Kulah. Fully self-powered electromagnetic energy harvesting system with highly efficient dual rail output. *IEEE Sensors Journal*, 12(6):2287–2298, 2012.

[56] Özge Zorlu, Emre Tan Topal, and Haluk Kulah. A vibration-based electromagnetic energy harvester using mechanical frequency up-conversion method. *IEEE Sensors Journal*, 11(2):481–488, 2011.

[57] Mingyi Liu, Rui Lin, Shengxi Zhou, Yilun Yu, Aki Ishida, Margarita McGrath, Brook Kennedy, Muhammad Hajj, and Lei Zuo. Design, simulation and experiment of a novel high efficiency energy harvesting paver. *Applied Energy*, 212:966–975, 2018.

[58] Zutao Zhang, Xingtian Zhang, Weiwu Chen, Yagubov Rasim, Waleed Salman, Hongye Pan, Yanping Yuan, and Chunbai Wang. A high-efficiency energy regenerative shock absorber using supercapacitors for renewable energy applications in range extended electric vehicle. *Applied Energy*, 178:177–188, 2016.

[59] S Palagummi and FG Yuan. An optimal design of a mono-stable vertical diamagnetic levitation based electromagnetic vibration energy harvester. *Journal of Sound and Vibration*, 342:330–345, 2015.

[60] Yan Chen, Tim E Pollock, and Armaghan Salehian. Analysis of compliance effects on power generation of a nonlinear electromagnetic energy harvesting unit; theory and experiment. *Smart Materials and Structures*, 22(9):094027, 2013.

[61] Issam Abed, Najib Kacem, Noureddine Bouhaddi, and Mohamed Lamjed Bouazizi. Multi-modal vibration energy harvesting approach based on nonlinear oscillator arrays under magnetic levitation. *Smart Materials and Structures*, 25(2):025018, 2016.

[62] David J Griffiths. Introduction to electrodynamics, 2005.

[63] Roszaidi Ramlan, MJ Brennan, BR Mace, and I Kovacic. Potential benefits of a non-linear stiffness in an energy harvesting device. *Nonlinear dynamics*, 59(4):545–558, 2010.

[64] Ivana Kovacic and Michael J Brennan. *The Duffing equation: nonlinear oscillators and their behaviour*. John Wiley & Sons, 2011.